

Infants display reduced NK cell responses in RSV and increased inflammatory responses in SARS-CoV-2 infections

Duygu Ucar

Duygu.Ucar@jax.org

Jackson Laboratories <https://orcid.org/0000-0002-9772-3066>

Asa Thibodeau

The Jackson Laboratory

Asuncion Mejias

Department of Infectious Diseases, St. Jude Children's Research Hospital <https://orcid.org/0000-0002-5983-8006>

Djamel Nehar-Belaid

Jackson Laboratory <https://orcid.org/0000-0001-6002-5021>

Radu Marches

The Jackson Laboratory for Genomic Medicine

Zhaohui Xu

St. Jude Children's Research Hospital <https://orcid.org/0000-0003-0645-1737>

Giray Eryilmaz

The Jackson Laboratory <https://orcid.org/0000-0003-3599-5207>

Steven Josefowicz

Weill Cornell Medicine <https://orcid.org/0000-0001-7453-779X>

Silke Paust

The Jackson Laboratory

Virginia Pascual

Weill Cornell Medicine <https://orcid.org/0000-0002-8806-8426>

Jacques Banchereau

Baylor Institute for Immunology Research

Octavio Ramilo


St. Jude Children's Research Hospital <https://orcid.org/0000-0002-0565-5239>

Article

Keywords:

Posted Date: January 13th, 2025

DOI: <https://doi.org/10.21203/rs.3.rs-5640872/v1>

License:  This work is licensed under a Creative Commons Attribution 4.0 International License.
[Read Full License](#)

Additional Declarations: There is **NO** Competing Interest.

Abstract

Respiratory syncytial virus (RSV) is the leading cause of lower respiratory tract infection hospitalizations in infants and poses a significantly higher risk of respiratory failure than SARS-CoV-2. The mechanisms underlying these differences remain unclear. We analyzed blood samples from infants (median age 2.3 months) with SARS-CoV-2 (n = 30), RSV (n = 19), and healthy controls (n = 17) using single-cell transcriptomics and epigenomics, and cytokine profiling. Both viruses triggered comparable interferon responses across PBMC subsets but differed in NK cell and inflammatory responses. Severe RSV cases showed reduced NK cell frequencies, lower *IFNG* expression, and decreased chromatin accessibility at T-BET and EOMES binding sites. RSV infections were also associated with increased CD4⁺ T_{EMRA}, memory T_{reg} and transitional B cells. In contrast, SARS-CoV-2 was characterized by stronger pro-inflammatory signatures, including increased NFκB pathway activity and higher serum TNF concentrations. These findings highlight distinct immune responses to RSV and SARS-CoV-2, providing insights that may inform clinical decisions.

INTRODUCTION

Respiratory viral infections including those caused by respiratory syncytial virus (RSV) and severe acute respiratory syndrome coronavirus 2 (SARS-CoV-2) pose significant risks to infants^{1–3}. Infants have developing immune systems that rely predominantly on innate immunity, along with smaller airways, making them more vulnerable to inflammation and severe respiratory morbidity⁴. RSV is a leading cause of lower respiratory tract infection, including bronchiolitis and pneumonia, leading to hospitalization in infants, and is the second leading cause of infant mortality globally^{5–8}. Conversely, the clinical presentation of SARS-CoV-2 infections in infants tend to be milder, with lower morbidity and hospitalization rates compared to RSV⁹. This contrast between these two respiratory viruses was particularly evident during the early stages of the COVID-19 pandemic. The biological mechanisms behind these differences remain poorly understood. Dissecting the immune responses of infants to these two respiratory viruses may help explain the observed clinical disparities.

RSV infections can significantly impact infant immune cells, disrupting the normal functions of T cells and macrophages and impairing their ability to effectively control the infection¹⁰. Our previous studies uncovered blood-driven transcriptional signatures of RSV in children and infants^{11,12}. Young children with mild disease had greater induction of interferon and plasma cell genes and decreased expression of inflammation and neutrophil genes compared to children with severe disease^{11,12}. Severe RSV disease was associated with increased numbers of HLA-DR^{low} monocytes and reduced interferon responses^{11–13}. Although these studies provided valuable insights into RSV disease signatures, bulk profiling lacked the resolution needed to identify cell-type-specific immune responses driving these signatures. Single-cell profiling overcomes this limitation, enabling the characterization of immune signatures at the cellular level.

Little is known about how SARS-CoV-2 virus interacts with the developing immune systems of infants. Infants with mild SARS-CoV-2-infection developed robust antibody responses, which persisted for months¹⁴. The nasal mucosal immune response in these infants was characterized by the presence of inflammatory cytokines, IFN α , and markers for Th17 cells and neutrophils¹⁴. In contrast, the immune response in the blood showed activation of innate cells and expression of ISGs, but without notable inflammation¹⁴. We recently observed significant changes in immune cell compositions in infants with moderate and severe SARS-CoV-2 infection, with most cell types displaying increased interferon-stimulated gene (ISG) expression¹⁵. Compared to adults, infants exhibited a similar ISG response in monocytes but a more pronounced ISG response in T and B cells, highlighting unique aspects of early-life immunity to SARS-CoV-2¹⁵. While interferon activation has been documented in both RSV and SARS-CoV-2 infections in infants^{11,12,14}, the extent to which these responses are comparable and the roles of other immune pathways, such as inflammation, remain unclear. Furthermore, while epigenetic mechanisms are critical in shaping immune responses to infectious diseases, their role in RSV and SARS-CoV-2 pathogenesis, particularly in infants, is not well understood.

To address these gaps, we recruited two cohorts of infants (median age: 2.3 months) infected with RSV (n = 30) or SARS-COV-2 (n = 19) across varying disease severities (mild, moderate, severe), alongside age-matched healthy controls (n = 17). We profiled peripheral blood mononuclear cells (PBMCs) using single cell RNA-sequencing (scRNA-seq) and single nucleus assay for transposase-accessible chromatin with sequencing (snATAC-seq) to investigate transcriptional and epigenetic responses.

RESULTS

Study design

From February 2019 through January 2022, we enrolled 49 infants and young children hospitalized with SARS-CoV-2 (n = 30; median IQR age: 1.9 [0.9–7.7] months) or RSV infection (n = 19; 2.8 [1.5–5.4] months) and obtained blood samples within 24 hours for peripheral blood mononuclear cell (PBMC) isolation and serum proteome analyses. We also included samples from a cohort of healthy controls (n = 17; 2.1 [1.8–8.4] months) enrolled before the COVID-19 pandemic. The cohorts were age- and sex-matched with the majority (89%) of infants being less than 12 months old (Fig. 1a, Extended Data Fig. 1a-c). The basic demographic and clinical characteristics of the 66 infants included in this study are summarized in Table S1.

Infants with COVID-19 were classified as subacute (n = 9); moderate (n = 12), or severe (n = 9) based on three criteria: (1) level of clinical care (oxygen administration, PICU care); (2) SARS-CoV-2 viral loads at admission, and (3) days post-exposure to an index COVID-19 case (Fig. 1b; Table S1). Infants in the subacute COVID-19 group had low viral loads and longer duration since exposure, with a median of 21 days. Children with moderate COVID-19 had high SARS-CoV-2 loads and were all hospitalized in the inpatient ward with respiratory tract symptoms and/or fever. Most (90%) infants in the severe COVID-19

group required PICU care for lower respiratory tract disease. Four of these infants were treated with dexamethasone, and classified as severe treated (referred to as “severe T”) to account for steroid effects on immune responses^{16,17}. All infants with acute RSV infection presented with respiratory symptoms and were classified as mild (n = 5), moderate (n = 7), or severe (n = 7) based on a standardized clinical disease severity score^{11,18,19} (Fig. 1c).

PBMCs were isolated and profiled using scRNA-seq (66 samples) and snATAC-seq (51 samples). After quality control and batch correction (Table S2, Extended Data Fig. 1d,e), scRNA-seq and snATAC-seq data yielded 364,131 and 233,563 cells, respectively (Fig. 1d,e). Major immune cell lineages were identified using marker gene expression and gene activity scores (Fig. 1d,e, Extended Data Fig. 1f). Detailed clustering and annotation within these lineages identified 48 distinct subsets in scRNA-seq (Extended Data Fig. 1f), of which 26 were also defined in the snATAC-seq dataset through label transfer (Extended Data Fig. 1g). Additionally, serum cytokines were analyzed using the Olink 96 Inflammation panel (n = 54 samples, including 37 infants from this cohort and 17 additional healthy controls) (Fig. 1a, Table S3).

Pro-Inflammatory cytokine responses differ between SARS-CoV-2 and RSV infections

Principal component analysis (PCA) of cytokine concentrations revealed clear distinctions in infants based on infection status (PC1) and infection type (PC2) (Fig. 1f). Key cytokines involved in inflammatory modulation, including IL-6, IL-10, and CXCL8 (IL-8), were elevated to comparable concentrations in both infections compared to healthy controls ($p_{\text{adj}} < 0.0011$) (Fig. 1g,h). IL-6 concentrations also correlated with RSV clinical disease severity scores (Pearson $r = 0.7$, $p_{\text{adj}} = 0.0075$; Extended Data Fig. 1h), consistent with our previous observations¹⁹. Virus-specific differences were also noted: SARS-CoV-2-infected infants exhibited increased concentrations of TNF, CCL8, and CXCL1 (Fig. 1g,h), whereas RSV-infected infants displayed increased levels of CASP8 (Fig. 1g), a molecule involved in initiating apoptosis and modulating inflammasome²⁰. These findings highlight both shared and unique cytokine responses in SARS-CoV-2 and RSV infections.

Myeloid cells mount strong interferon transcriptional responses in both infections

Myeloid cells were annotated into seven subsets: ISG^{hi} and ISG^{lo} CD14⁺ monocytes (n = 9,086, n = 17,730), ISG^{hi} and ISG^{lo} CD16⁺ monocytes (n = 5,569, n = 3,772), ISG^{hi} CD163⁺ monocytes (n = 3,800), dendritic cells (DCs) (n = 855), and plasmacytoid dendritic cells (pDCs) (n = 770) (Fig. 2a). The frequencies of DCs and pDCs were lower ($p_{\text{adj}} < 0.007$ for DCs, $p_{\text{adj}} < 0.067$ for pDCs) in both infections compared to healthy controls (Fig. 2b, Extended Data Fig. 2a).

DC clustered into monocyte-derived DCs (mo-DCs) (*CD14* expression, $n = 389$), conventional DC type-2 (cDC2) (*CD1C*, $n = 391$), cDC type-1 (cDC1) (*CLEC9A*, $n = 50$), and $AXL^+ SIGLEC6^+$ DCs (*AXL* and *SIGLEC6*, $n = 25$) (Fig. 2c). Mo-DCs, cDC1s and $AXL^+ SIGLEC6^+$ DCs were less frequent ($p_{adj} < 0.051$) in both infections, while cDC2 frequency was lower ($p_{adj} = 0.042$) only in SARS-CoV-2 infection (Extended Data Fig. 2b). High ISG (e.g., *ISG15*) expression was observed in infected infants (Extended Data Fig. 2c). Cumulative transcriptional ISG scores confirmed significantly higher ISG expression in infected infants ($p_{adj} < 0.001$; Extended Data Fig. 2d, Table S4).

$CD14^+$ monocytes were more frequent in RSV-infected infants compared to healthy controls ($p_{adj} = 0.035$; Fig. 2e, Extended Data Fig. 2a). Three ISG^{hi} subsets were identified within monocytes: $ISG^{hi} CD14^+$ monocytes, $ISG^{hi} CD163^{hi} CD14^+$ monocytes, and $ISG^{hi} CD16^+$ monocytes. These ISG^{hi} clusters were more frequent in acute infections but not in the subacute COVID-19 group (Fig. 2f, Extended Data Fig. 2e). The $ISG^{hi} CD163^{hi} CD14^+$ monocyte subset was exclusively found in four dexamethasone-treated infants with severe COVID-19 (severe T, Fig. 2f). Although these cells retained ISG expression, levels were lower than those in $ISG^{hi} CD14^+$ monocytes, suggesting that dexamethasone attenuates interferon responses in monocytes (Fig. 2g).

Differential gene expression analyses revealed 560 and 601 upregulated genes in total $CD14^+$ and $CD16^+$ monocytes, respectively, including ISGs (e.g., *IFI44*, *IFI44L*, *IFI27*, *IFITM2*, and *OASL*) and inflammatory molecules (Fig. 2h, Extended Data Fig. 2f-h, Table S5). Downregulated genes were enriched in pathways related to protein synthesis and transcription (Extended Data Fig. 2g-h). ISG scores were consistently high across acute infections, with no significant differences between the two diseases or among disease severities (Fig. 2i, Extended Data Fig. 2i). Together, these results demonstrate that both SARS-CoV-2 and RSV infections induce robust interferon transcriptional responses in DCs, pDCs, and monocytes, regardless of disease severity.

Lower *IL1B* expression in severe RSV and higher *NFKB* gene expression in COVID-19

To investigate pro-inflammatory signatures, we first examined *IL1B* expression. In $CD14^+$ monocytes, *IL1B* was lower in RSV-infected infants compared to healthy controls ($p_{adj} = 0.046$), with the decrease primarily driven by infants with severe RSV disease ($p_{adj} = 0.005$, Fig. 2j, Extended Data Fig. 2j). $CD14^+$ monocytes co-expressing *ISG15* and *IL1B* were more frequent in infected infants, regardless of disease severity (Fig. 2k,l).

Next, we analyzed the NF- κ B pathway genes (Table S4), which were upregulated in SARS-CoV-2-infected infants compared to healthy controls ($p_{adj} = 0.0046$ for $CD14^+$ monocytes and $p_{adj} < 0.001$ for $CD16^+$ monocytes) and RSV-infected infants ($p_{adj} = 0.0016$ for $CD14^+$ monocytes and $p_{adj} < 0.001$ for $CD16^+$ monocytes) (Fig. 2m, Extended Data Fig. 2k). Genes within this pathway, including *IL1A* and *TNF*, were more expressed in moderate and severe COVID-19 cases compared to RSV (Extended Data Fig. 2l-m).

Steroid treatment modulated these inflammatory responses. Both *IL1B* expression and NF- κ B pathway scores were reduced in steroid-treated (severe T) infants (Extended Data Fig. 2j,k). To further explore these effects, we compared the transcriptomes of CD14⁺ monocytes from severe and severe T COVID-19 cases (Table S5). In the treated infants, *NFKBIE* and *NFKB2* were downregulated, while *CD163* and *IL1R2* were upregulated (Fig. 2n), suggesting a shift toward an anti-inflammatory state.

In summary, SARS-CoV-2 and RSV induced distinct inflammatory profiles in monocytes. *IL1B* expression was downregulated in infants with severe RSV infection, whereas NF- κ B pathway genes were upregulated with SARS-CoV-2 infection.

Durable epigenetic ISG signatures in infant monocytes

We investigated the epigenomes of CD14⁺ (n = 22,866 cells) and CD16⁺ monocytes (n = 6,255) in both infections (Fig. 3a). In CD14⁺ monocytes, we identified 2,454 differentially accessible peaks (992 opening, 1,462 closing) between healthy and infected infants (Fig. 3b). Similarly, in CD16⁺ monocytes, we identified 1,122 differentially accessible peaks (411 opening, 711 closing; Extended Data Fig. 3a). Opening peaks were annotated to multiple ISGs (e.g., *MX1*, *IFITM3*, and *IFI44L*) and enriched for interferon modules (Fig. 3b, Extended Data Fig. 3a,b, Table S6).

We calculated an epigenetic ISG score based on chromatin accessibility levels at ISG loci in monocytes (Fig. 3c, Extended Fig. 3c). This score was higher in all infected infants, including those in the subacute COVID-19 group ($p_{\text{adj}} < 0.014$, Fig. 3c). To assess the persistence of this epigenetic interferon activity, we reanalyzed ATAC-seq profiles of CD14⁺ monocytes from convalescent adults 2–4 months post-SARS-CoV-2 infection²¹. Using infant-derived ATAC-seq peaks, we found that epigenetic interferon activity persisted in adults, with higher scores observed in severe COVID-19 cases compared to healthy controls ($p_{\text{adj}} < 0.001$) and mild COVID-19 cases ($p_{\text{adj}} = 0.101$; Extended Data Fig. 3d). These results suggest that SARS-CoV-2 induces durable epigenetic ISG signatures in monocytes in both infants and adults.

To further link chromatin accessibility changes to gene expression, we performed Domains of Regulatory Chromatin (DORC) analysis²² (Table S7). *ISG15* was associated with 13 peaks that cumulatively correlated with its expression (Pearson $r = 0.65$, $p = 7.0 \times 10^{-7}$; Fig. 3d,e). DORC scores for *ISG15* were elevated ($p_{\text{adj}} < 0.008$) in acute cases of both infections (Fig. 3f). In contrast, *IL1B* DORC scores were reduced in steroid-treated severe COVID-19 cases and severe RSV cases ($p_{\text{adj}} = 0.032$ and 0.006 , respectively; Fig. 3g-h).

To study changes in transcription factor (TF) binding activity, we used chromVAR²³ (Fig. 3i-m, Extended Data Fig. 3e-h). Binding sites for interferon regulatory factors (IRF) were more accessible in RSV-infected infants compared to SARS-CoV-2-infected infants in both CD14⁺ and CD16⁺ monocytes (Fig. 3i-l, Extended Data Fig. 3e-g). Despite this, IRF genes were upregulated in response to both SARS-CoV-2 and RSV infections (Extended Data Fig. 3i,j). Conversely, binding sites for NF- κ B family factors were more

accessible in SARS-CoV-2-infected infants, particularly in CD16⁺ monocytes (Fig. 3m, Extended Data Fig. 3h).

In summary, we observed a persistent epigenetic interferon response in infant monocytes that extended beyond transcriptional changes. Virus-specific differences were evident in TF binding site accessibility, with increased IRF accessibility in RSV and increased NF- κ B/REL factor accessibility in SARS-CoV-2.

Reduced NK cell frequencies and downregulation of IFNG/IFNG-AS1 in severe RSV

We identified three NK cell subsets: mature CD56^{dim} (*FCGR3A*, $n = 16,300$), immature CD56^{bright} (*NCAM1*, $n = 3,315$), and proliferating NK cells (*MKI67* and *PCNA*, $n = 1,427$) (Fig. 4a). The frequency of CD56^{bright} NK cells was lower ($p_{\text{adj}} = 0.0499$) in all RSV-infected infants compared to healthy controls, while the frequency of CD56^{dim} NK cells was lower ($p_{\text{adj}} = 0.01$) specifically in severe RSV cases (Fig. 4b,c, Extended Data Fig. 4a,b). Conversely, the frequency of proliferating NK cells was increased in SARS-CoV-2 infected infants (Fig. 4b, Extended Data Fig. 4b). *ITGA4*, a marker for lung migration, was upregulated in RSV-infected infants across all NK cell subsets (Extended Data Fig. 4cd), suggesting enhanced NK cell recruitment to the lungs with RSV.

ISG scores were higher across all NK subsets in infants with acute SARS-CoV-2 or RSV infections ($p_{\text{adj}} < 0.0044$, Fig. 4d, Extended Data Fig. 4e-g). Cytotoxic genes, *GZMB* and *PRF1*, were also upregulated in both infections within CD56^{dim} and CD56^{bright} NK cells (Extended Data Fig. 4h). NK cells produce interferon gamma (IFN- γ) encoded by the *IFNG* gene, which is regulated by the long noncoding RNA *IFNG-AS1*²⁴. *IFNG*, expressed primarily in CD56^{dim} NK cells, was downregulated in severe RSV and steroid-treated severe COVID-19 ($p_{\text{adj}} = 0.019$; Fig. 4e). *IFNG-AS1*, expressed primarily in CD56^{bright} NK cells, was downregulated in moderate and severe RSV cases ($p_{\text{adj}} < 0.004$, Fig. 4f). Expression levels of *IFNG* and *IFNG-AS1* inversely correlated with RSV disease severity, with lower levels observed in infants with more severe disease (Pearson $r = -0.49$ and -0.50 , $p = 0.034$ and 0.30 for CD56^{dim} and CD56^{bright} NK cells respectively; Fig. 4e,f). In summary, severe RSV infection is associated with reduced frequencies of NK cells and downregulated *IFNG* expression, highlighting impaired NK cell responses in these cases.

T-BET and EOMES binding site accessibility is associated with IFNG expression in NK cells

We captured CD56^{dim} NK ($n = 12,917$) and CD56^{bright} NK ($n = 2,309$) subsets in snATAC-seq data (Fig. 4g). ChromVAR analysis revealed increased IRF binding site accessibility in both NK subsets for both infections (Table S8). However, an RSV-specific decline in chromatin accessibility at T-box family TF binding sites, including key NK cell maturation and IFN- γ production regulators TBX21 (T-BET) and EOMES²⁵, was observed in both NK subsets (Fig. 4h,i,j, Extended Data Fig. 5a,b,c). This decline was more pronounced in moderate and severe RSV cases, particularly in CD56^{bright} NK cells ($p_{\text{adj}} < 0.011$, Fig. 4k,l). Chromatin accessibility at EOMES binding sites was inversely correlated with RSV disease severity, with the lowest accessibility observed in infants with the most severe disease (Extended Data Fig. 5d,e).

Notably, these reductions occurred independently of *TBX21* and *EOMES* expression levels (Extended Data Fig. 5f-g).

A regulatory ATAC-seq peak containing T-BET and EOMES motifs, located 4kb upstream of the *IFNG* transcription start site (TSS), was accessible in both NK subsets (Fig. 4m). Chromatin accessibility at this locus inversely correlated with RSV disease severity in CD56^{dim} NK cells (Pearson $r = -0.49$, $p_{\text{adj}} < 0.044$; Extended Data Fig. 5h), with the lowest accessibility observed in the most severe cases (Fig. 5m, Extended Data Fig. 5i). Additionally, accessibility of this locus was positively correlated with *IFNG* and *IFNG-AS1* expression in both NK subsets (Fig. 4n, Extended Data Fig. 5j). These findings suggest that RSV disease severity is linked to impaired accessibility at regulatory loci critical for *IFNG* expression in NK cells.

ISGs are upregulated in CD8⁺/cytotoxic T cells in both SARS-CoV-2 and RSV

CD8⁺/cytotoxic T cells clustered into eight subsets: ISG^{lo} naive CD8⁺ T ($n = 38,397$), ISG^{hi} naive CD8⁺ T (*ISG15*, $n = 3,852$), GZMK^{hi} CD8⁺ T (*GZMK*, $n = 2,693$), CD8⁺ terminal effector memory T (T_{EMRA}) (*GZMB*, $n = 2,759$), mucosal-associated invariant T (*KLRB1*, MAIT) ($n = 2,296$), proliferating T cells (*MKI67*, $n = 796$), $\gamma\delta$ T (*TRDC* and *TRGC2*, $n = 2,349$), and CD8⁺ $\gamma\delta$ T ($n = 1,378$) (Fig. 5a, Extended Data Fig. 6a). The frequency of ISG^{hi} naive CD8⁺ T cells was higher in RSV or SARS-CoV-2 infected infants ($p_{\text{adj}} < 0.001$, Fig. 5b, Extended Data Fig. 6b,c). ISG scores were increased across all subsets during acute disease (Extended Data Fig. 6d-j). However, no significant differences in ISGs were observed between RSV and SARS-CoV-2 or across disease severities (Table S5). The frequency of proliferating T cells, both CD8⁺ and CD4⁺, was higher in RSV-infected infants ($p_{\text{adj}} < 0.021$ compared to controls; $p_{\text{adj}} < 0.064$ compared to COVID-19; Extended Data Fig. 6c,k,l). The frequency of $\gamma\delta$ T cells was lower in SARS-CoV-2 ($p_{\text{adj}} = 0.024$, Fig. 5b, Extended Data Fig. 6c), consistent with reports from SARS-CoV-2-infected adults and children^{26–28}.

The most notable epigenetic differences between RSV and SARS-CoV-2 were observed in naive CD8⁺ T cells (Extended Data Fig. 7a,b). In these cells, binding sites for AP-1 transcription factors (e.g., FOS, FOSL2, and JDP2) and NF- κ B member REL were more accessible in SARS-CoV-2-infected infants compared to RSV-infected infants (Extended Data Fig. 7b). NF- κ B pathway genes were both upregulated and more accessible in SARS-CoV-2-infected infants compared to RSV-infected infants (Fig. 5c,d, Extended Data Fig. 7c,d).

In summary, infants mount robust interferon responses in CD8⁺/cytotoxic T cells in RSV and SARS-CoV-2 infections. However, SARS-CoV-2-infected infants showed greater chromatin accessibility and expression of pro-inflammatory NF- κ B and AP-1 factors.

RSV-infected infants have increased CD4⁺ T_{EMRA} and memory T_{reg} cells

CD4⁺ T cells clustered into four subsets: ISG^{lo} naive CD4⁺ T (*CCR7* 133,880) and ISG^{hi} naive CD4⁺ T (*ISG15*, n = 29,969), memory CD4⁺ T (*S100A4*, n = 14,048), and T_{reg} (*FOXP3*, n = 10,328) cells (Fig. 5e). While the overall frequency of naive CD4⁺ T cells did not change with infections, the frequency of ISG^{hi} naive CD4⁺ T cells increased in infected infants ($p_{\text{adj}} < 0.001$, Fig. 5f). No differences were observed in memory CD4⁺ T and T_{reg} cell frequencies (Fig. 5f).

Memory CD4⁺ T cells further clustered into eight subsets: CD4⁺ central memory T (T_{CM}) (*CCR7*, n = 5,557), CD4⁺ T_{EMRA} (*NKG7*, n = 102), ISG^{lo} T follicular helper-like (Tfh) (*CXCR5*, n = 3,691), ISG^{hi} Tfh (*ISG15*, n = 1,005), Th1 (*IFNG-AS1*, n = 399), Th2 (*GATA3-AS1*, n = 234), Th17 (*RORC*, n = 347), and Th22 (*CCR10*, n = 348) cells (Fig. 5g,h, Extended Data Fig. 7e-g). The total Tfh cell frequencies were comparable across the three clinical groups, however, ISG^{hi} Tfh-like cells were increased in both infections ($p_{\text{adj}} < 0.001$, Fig. 5i, Extended Data Fig. 7h,i). CD4⁺ TEMRA cell frequencies were higher in RSV-infected infants ($p_{\text{adj}} < 0.003$, Fig. 5i, Extended Data Fig. 7i). Th22-like cell frequencies were higher in RSV-infected infants compared to SARS-CoV-2-infected infants ($p_{\text{adj}} = 0.013$, Fig. 5i).

T_{reg} cells clustered into three subsets: ISG^{lo} naive T_{reg} (*CCR7*, n = 8,589), ISG^{hi} naive T_{reg} (*ISG15*, n = 772), and memory T_{reg} cells (*S100A4*, n = 967) (Fig. 5j). While total naive Treg frequencies remained unchanged, ISG^{hi} T_{reg} cells were more frequent in infected infants ($p_{\text{adj}} < 0.001$, Fig. 5k, Extended Data Fig. 7j,k). Memory T_{reg} cell frequencies were higher in RSV-infected infants compared to other groups ($p_{\text{adj}} < 0.0016$, Fig. 5k, Extended Data Fig. 7k). Most CD4⁺ T cell subsets showed comparably increased ISG scores in both infections (Extended Data Fig. 7l, 8a-i).

The most notable epigenetic differences between RSV and SARS-CoV-2 were observed in naive CD4⁺ T cells (Extended Data Fig. 8j). IRF and STAT binding site accessibility was increased in both infections (Extended Data Fig. 8k), while pro-inflammatory AP-1 and NF-κB binding site accessibility was increased in SARS-CoV-2-infected infants (Extended Data Fig. 8k). Naive CD4⁺ T cells from SARS-CoV-2-infected infants showed higher activity for NF-κB pathway genes at both epigenetic and transcriptional levels ($p_{\text{adj}} < 0.022$, Extended Data Fig. 8l-n).

In summary, both RSV and SARS-CoV-2 infections induced interferon responses across all CD4⁺ T cell subsets. RSV-infected infants had higher frequency of CD4⁺ T_{EMRA} and memory T_{reg} cells and reduced NF-κB activity.

B cells display increased ISGs in both infections

B cells were clustered into six subsets: naive B (*CCR7*, $n = 33,728$), transitional B (TrB) (*MME*, $n = 17,194$), memory B (*CD27*, $n = 6,330$), AIM2^{hi} memory B (*AIM2*, $n = 841$), plasmablasts (*JCHAIN*, $n = 466$) and double-negative-2 (DN2) B ($n = 441$) cells (Fig. 6a). The frequency of TrB cells was higher in RSV-infected infants ($p_{\text{adj}} = 0.036$, Fig. 6b). No other cell compositional differences were observed across B cell subsets (Extended Data Fig. 9a). Clustering of naive B and TrB cells identified ISG^{hi} subsets, both of which were increased in infected infants ($p_{\text{adj}} < 0.0037$) (Fig. 6c-f, Extended Data Fig. 9b,c). ISG scores were higher across all B cell subsets in infected infants ($p_{\text{adj}} < 0.05$, Extended Data Fig. 9d-i). Epigenetic differences between RSV and SARS-CoV-2 were observed in TrB cells (Fig. 6g,h). In RSV-infected infants, pro-inflammatory AP-1 TFs had reduced chromatin and expression levels (Fig. 6h,i Extended Data Fig. 9j,k).

A subset of naïve B cells highly expressed *FKBP5* (Fig. 6c, Extended Data Fig. 9c), which encodes the FK506-binding protein 51 that interacts with glucocorticoid receptors²⁹. The majority (88%) of cells in this cluster originated from steroid-treated COVID-19 infants ($n = 4$; Extended Data Fig. 9l), suggesting a drug-induced effect on B cells. This *FKBP5*^{hi} B cell cluster exhibited lower interferon responses (Extended Data Fig. 9m). Comparisons between severe and severe T COVID-19 groups revealed 493 differentially expressed genes and 291 differentially accessible peaks across seven immune cell subsets (Extended Data Fig. 10a, Table S4,5). Some genes, such as *FKBP5*, were consistently upregulated across multiple immune cell subsets, while others, such as *CD163* and *IL1R2* in monocytes, were induced in a cell-type-specific manner (Extended Data Fig. 10b).

In summary, B cells mounted strong interferon responses during RSV and SARS-CoV-2 infections. TrB cells were particularly affected in RSV, showing increased frequencies along with reduced accessibility and expression of AP-1 transcription factors.

DISCUSSION

This study provides comprehensive multi-modal insights into the immune responses of infants to SARS-CoV-2 and RSV infections, revealing both shared and virus-specific immune signatures. Both viruses induced robust interferon responses across PBMC subsets, a hallmark of antiviral immunity, evidenced by the upregulation of interferon-stimulated genes (Fig. 6j) and increased chromatin accessibility at interferon regulatory factor (IRF) binding sites (Fig. 6k). However, we observed key differences in i) inflammatory responses, ii) epigenetic remodeling, and iii) NK and iv) adaptive cell subsets that might underlie the divergent clinical outcomes of these infections (Fig. 6l).

Inflammation emerged as a critical point of divergence between the two infections. SARS-CoV-2 induced strong pro-inflammatory responses, characterized by elevated serum concentrations of TNF, IL-6, and IL-8, alongside upregulated NF- κ B pathway activity in monocytes, NK cells, and T cells. These findings are consistent with the acute inflammatory response observed in severe COVID-19 cases³⁰. In contrast, RSV infections were associated with reduced expression and chromatin accessibility of *IL1B* in CD14⁺

monocytes, particularly in severe cases, and lower serum concentrations of TNF, IL6, IL8 in serum, indicating a more tempered inflammatory response. Previous findings from our group demonstrated an inverse correlation between innate immunity cytokine levels in nasal wash and plasma and RSV disease severity^{18,19,31}. Moreover, infants with severe RSV exhibited increased numbers of HLA-DR^{low} monocytes¹², often associated with immune suppression. Our findings further revealed transcriptional and epigenetic impairments in circulating monocytes in severe RSV cases, underscoring the critical role of robust innate immune responses in mitigating RSV severity.

NK cell dysregulation was a hallmark of severe RSV infection. The reduction in NK cell frequencies, coupled with impaired *IFNG* expression and diminished chromatin accessibility at T-BET and EOMES binding sites (Fig. 6k,l). NK cell recruitment to the lungs during severe RSV infection has been previously reported³², potentially contributing to their depletion in peripheral blood. While reduced *IFNG* expression in total PBMCs has been previously reported in infants with severe RSV³³, the cellular source of this reduction remained unclear until now.

Epigenetic analyses revealed ISG signatures in monocytes in both infections, including subacute COVID-19 cases, suggesting a durable epigenetic memory of interferon responses. This is consistent with adult studies demonstrating persistent chromatin remodeling months after SARS-CoV-2 infection^{21,34}. Notably, the ISGs epigenetically activated in infants mirrored those observed in adults recovering from COVID-19 and were correlated with disease severity. In RSV-infected infants, increased IRF binding site accessibility in monocytes pointed to a distinct regulatory mechanism potentially modulated by viral factors affecting IRF binding site dynamics. These epigenetic changes in RSV-infected infants might help explain the virus's long term respiratory morbidity (e.g., wheezing and asthma)³⁵⁻³⁷. These findings underscore the critical role of epigenetics in shaping immune responses and infant immunity.

Adaptive immune responses also differed between the infections. RSV infection was associated with increases in CD4⁺ TEMRA cells,, which are expanded in other infectious diseases such as Dengue virus and HIV^{38,39}, where they contribute to the elimination of infected cells. Although CD4⁺ TEMRA cells primarily function as effector cells, they can exhibit immunosuppressive properties in chronic infections like HIV³⁹. In RSV, the concurrent expansion of memory Tregs and CD4⁺ TEMRA cells may reflect the virus's capacity to induce immune suppression. The increase in TrB cells in RSV infection may represent a compensatory mechanism for the loss of circulating B cells, as previously observed in RSV cases¹¹. In contrast, SARS-CoV-2 infections were characterized by heightened pro-inflammatory transcription factor activity in naive CD4⁺ and CD8⁺ T cells, consistent with the virus's stronger inflammatory profile.

In severe COVID-19 cases treated with dexamethasone, distinct transcriptional and epigenetic signatures were observed across multiple immune cell types, reflecting the modulatory effects of corticosteroids in infants, similar to findings in adults^{16,17}. Dexamethasone-treated infants exhibited reduced expression of NF-κB pathway genes and *IL1B*, consistent with the drug's anti-inflammatory effects. Simultaneously, these infants displayed upregulation of anti-inflammatory markers such as *CD163* and *IL1R2*. Notably,

while interferon responses were dampened, they were not entirely suppressed, indicating a complex interplay between inflammation control and antiviral defense.

While this study demonstrates the utility of advanced single-cell and multi-omics approaches in uncovering nuanced immune responses of infants to viral infections, it is limited by its cross-sectional design and relatively small sample sizes for certain clinical groups. Longitudinal studies are needed to evaluate the persistence and functional consequences of the observed transcriptional and epigenetic changes. Future research should incorporate respiratory tract samples to better understand localized immune responses at the primary site of infection. However, repeated invasive sampling in this age group presents significant challenges.

This study highlights the distinct immune responses of infants to SARS-CoV-2 and RSV infections, driven by differences in inflammation, NK cell responses, and epigenetic regulation. These findings deepen our understanding of viral pathogenesis in infants and pave the way for guided clinical decision making to mitigate the burden of these infections in this vulnerable population.

METHODS

Study Design

SARS-CoV-2 and RSV Cohorts

A convenience sample of children < 2 years of age hospitalized with COVID-19 or respiratory syncytial virus (RSV) infection were prospectively enrolled at Nationwide Children's Hospital (NCH) in Columbus, Ohio, USA from February 2019 through January 2022. Blood (2.5-5 mL) and nasopharyngeal samples were obtained within 24 hours of hospitalization for multiomic analyses and SARS-CoV-2 and RSV quantitation by real-time polymerase chain reaction (PCR)⁴⁰. During the study period all children hospitalized at NCH, irrespective of the presence of symptoms, underwent nasopharyngeal SARS-CoV-2 testing using a PCR assay per standard of care as described⁴¹. For RSV infants, testing was performed at the discretion of the attending physician via multiplex PCR panel, and children were excluded if they had any underlying conditions (i.e prematurity, congenital heart disease, chronic lung disease) or use of immunomodulatory drugs including systemic steroids > 5 days within 2 weeks of presentation. At enrollment, we collected demographic and clinical information using a standardized questionnaire designed for the study, and information transferred to a secure database (REDCap). The information collected included duration of illness or time since exposure to an index case, and standard parameters of disease severity including oxygen administration, pediatric intensive care unit (PICU) admission, duration of hospitalization, and administration of systemic therapies including steroids. In addition, we used a standardized clinical disease severity score (CDSS) for infants with RSV infection as previously reported^{31,40}. This score was not applied to infants with COVID-19 due to their differing clinical presentations.

Healthy Controls

As a reference for all immune assays, we also included in the study a cohort of age-matched healthy control infants with no respiratory symptoms or treated with antibiotics within two weeks of enrollment. All healthy controls were enrolled pre-pandemic. Healthy controls were typically enrolled in the operating room while undergoing minor scheduled surgical procedures not involving the respiratory tract, or at the primary care offices during well-child visits.

This study was approved by the Nationwide Children's Hospital (NCH) IRB (18–00591). Written informed consent was obtained from all children's guardians before study participation. Further clinical details of all participants are summarized in Table S1.

PCR Assays for SARS-CoV-2 Viral loads

Nasopharyngeal (NP) swabs were collected at enrollment, placed in viral transport media, transported immediately to the laboratory, aliquoted and stored at -80°C . Similarly, blood samples were collected in EDTA tubes (BD Vacutainer, Franklin Lakes, NJ, USA), centrifuged, and aliquots of plasma were stored at -80°C until processed in batches. Viral RNA was extracted from 200 microliters of NP or plasma samples using the QIAcube HT instrument (Qiagen Inc, Germantown, MD, USA) and eluted into 100 microliter volume. In brief, SARS-CoV-2 viral loads were measured using a two-step reverse-transcription (RT) quantitative PCR assay targeting the conserved region of the N1 gene as described⁴¹. SV loads were measured by quantitative real-time PCR targeting the N gene, as described³¹. Standards and negative controls were included and tested with each PCR assay.

Cytokine Processing

A panel of 92 cytokines was analyzed with Olink at the Olink Boston Laboratory for 54 samples ($n = 37$ from this cohort, $n = 17$ additional healthy controls) over two separate runs. Bridge normalization from OlinkAnalyze R package⁴² was applied to adjust values for comparisons between runs.

Sample processing for scRNA-seq

PBMCs were thawed quickly at 37°C and into DMEM supplemented with 10% FBS. Cells were quickly spun down at 400 g, for 10 min. Cells were washed once with 1 x PBS supplemented with 0.04% BSA and finally re-suspended in 1 x PBS with 0.04% BSA. Viability was determined using trypan blue staining and measured on a Countess FLII. Briefly, 12,000 cells were loaded for capture onto the Chromium platform using the single cell 3' gene expression reagent kit (v3 or v3.1) (10x Genomics). Following capture and lysis via Chromium Chip G, cDNA was synthesized and amplified (12 cycles) as per manufacturer's protocol (10x Genomics, protocols CG000204; CG000315). Amplified cDNA and libraries

were checked for quality on Agilent 4200 TapeStation, quantified by KAPA qPCR, and sequenced on an Illumina NovaSeq 6000 targeting 100,000 raw read pairs per cell.

Sample processing for snATAC-seq

For single nucleus ATAC sequencing (snATAC-seq) experiments, viable single cell suspensions from each sample were used to generate snATAC-seq data using the 10x Chromium platform according to the manufacturer's protocols (10x Genomics, protocols CG000169; CG000168). Briefly, > 100,000 cells from each sample were centrifuged and the supernatant was removed without disrupting the cell pellet. Lysis Buffer was added for 5 minutes on ice to generate isolated and permeabilized nuclei, and the lysis reaction was quenched by dilution with Wash Buffer. After centrifugation to collect the washed nuclei, diluted Nuclei Buffer was used to re-suspend nuclei at the desired nuclei concentration as determined using a Countess II FL Automated Cell Counter and combined with ATAC Buffer and ATAC Enzyme to form a Transposition Mix. Transposed nuclei were immediately combined with Barcoding Reagent, Reducing Agent B and Barcoding Enzyme and loaded onto a 10x Chromium Chip H for droplet generation followed by library construction. The barcoded sequencing libraries were subjected to bead clean-up and checked for quality on an Agilent 4200 TapeStation, quantified by KAPA qPCR, and pooled for sequencing on an Illumina NovaSeq 6000 (2x50bp libraries).

scRNA-seq data processing

Reads from scRNA-seq were aligned (10x Genomics GRCh38 reference 2020-A) and processed using Cell Ranger v6.1.2⁴³. Ambient RNA corrected matrices were obtained by applying SoupX version 1.6.2⁴⁴. Multiplets were removed using Scrublet version 0.2.3⁴⁵ with the following parameters: Doublet Rate = 0.06, Min Counts = 2, Min Cells = 3, Min Gene Variability PCTL = 85, Number of PCs = 30. High-quality cells from each sample were selected using the following selection criteria: 1) mitochondrial percentage: > 1%; < 20%, 2) molecules detected: > 2000; < 25000, and 3) number of genes detected: ≥ 500 , resulting in a total of 389,281 high-quality cells.

In addition to the above cell selection protocols, we separated low and high quality cells by applying unsupervised clustering on the following features: 1) number of molecules, 2) number of genes detected, 3) mitochondria read percentage, 4) ribosomal gene percentage, 5) multiplet score (Scrublet) and 6) multiplet annotation (Scrublet). All cells were clustered by applying Uniform Manifold Approximation and Projection (UMAP) followed by clustering *via* HDBSCAN⁴⁶. Using this approach, 3 clusters were associated with low quality or multiplet cells, overlapping 99% with previous criteria and covering 22% of all low quality cells identified in the previous step. An additional 53 low quality cells were identified, resulting in 389,228 high-quality cells (2000–9161 per sample) before manual filtering.

Ambient mRNA corrected count matrices filtered for the remaining high quality cells from each sample were log normalized in Scanpy (version 1.9.1)⁴⁷ using *normalize_total(target_sum = 1e4)* and *log1p*

functions. Scanpy objects from each sample were concatenated into a single object for further processing. Low expressed genes were filtered using the *filter_genes(min_cells = 5)* and highly variable genes were identified using *highly_variable_genes()*. Highly variable genes were scaled using *scale(max_value = 10)* for Principle Component Analysis (PCA): *PCA(svd_solver='arpack', n_comps = 50)*. Principle components were then adjusted for batch effects by applying Harmony⁴⁸ using *harmony_integrate()* in Scanpy. Batch corrected PC values were then projected onto UMAP space and clustered using the Leiden clustering in Scanpy.

scRNA-seq cluster annotation

Cells from scRNA-seq were manually curated and annotated using two rounds of clustering and annotation. In each round, cells were divided into major immune cell lineages (myeloid, B cell, CD4⁺ T Cell, and NK/CD8⁺ and cytotoxic T cells) which were further clustered depending on the granularity required to describe known PBMC subsets. The number of components (adjusted PCA values from harmony) and resolution (Leiden) of clusters were adjusted as necessary depending on the detection of clusters representing known subsets. Clusters were excluded based on the presence of markers from multiple PBMC subsets (i.e. multiplets), red blood cell markers, or high mitochondrial gene percentages. The majority of cells were filtered in the first round, which was focused on identifying clusters for exclusion using the criteria described. Cells remaining after the first round of clustering were re-clustered by reapplying PCA (components = 100) and Harmony for a second round of curation and annotation. In the second round, any remaining multiplet clusters were excluded, and cells were annotated based on known marker genes of known immune cell types. Clusters showing high *ISG15* expression were annotated as ISG^{hi}. For CD14⁺ and CD16⁺ monocytes, ISG^{hi} clusters were selected based on scaled *ISG15* expression > 1.

Memory CD4⁺ T Cell Annotation

Memory CD4⁺ T cells were selected and processed using Seurat (version 5.1.0). Highly variable genes were selected with the FindVariableFeatures function using the following parameters: *selection.method="vst"* and *nfeatures = 2000*. RunPCA was applied and batch corrected using Harmony using the first 50 components. Clusters were obtained using Leiden with resolution = 1. Density plots were generated using Nebulosa (version 1.14.0)⁴⁹ for known memory CD4⁺ T markers for annotations.

Cell frequency comparisons

Cell frequencies were calculated as a percentage of cells within the subset out of the total number of PBMCs in the sample. Comparisons between Healthy, COVID-19 (moderate and severe), and RSV (mild, moderate and severe) were calculated using Dunn's multiple comparisons test for all pairwise

comparisons. Comparisons between clinical groups were calculated using Mann Whitney rank-sum tests for each group against healthy controls followed by Benjamini/Hochberg FDR correction for multiple comparisons.

Differential gene expression analysis

Aggregated raw gene expression count matrices were obtained for each annotated subset, merging ISG^{hi} and ISG^{lo} subsets and related small subsets (e.g., cDC1s with cDC2s etc) as described in Table S5. CD163^{hi} monocytes resembled CD14⁺ monocytes and were merged with CD14⁺ monocytes to capture differences between severe and severe T COVID-19 groups. For each comparison, samples with fewer than 25 cells in the respective population were excluded. Genes were excluded if fewer than 3 samples had expression in greater than 20% of cells. Sample and gene filtered count matrices were then normalized using *filterByExpr* and *calcNormFactors* functions in EdgeR (version 3.36.0)^{50–52}. Differential expression analyses were performed using *estimateDisp* and *glmQLFTest* functions, using batch, sex, and age as covariates. All pairwise comparisons between clinical group as well as combined Healthy, COVID-19 (moderate and severe), and RSV (mild, moderate and severe) comparisons were performed for each annotated subset that had enough samples remaining after filtering to run EdgeR.

Module analysis

Module enrichments were obtained using genes sets obtained from Altman et al⁵³. Briefly, genes were separated into upregulated and downregulated categories based on differential expression analyses. Overlaps with gene modules were tested for statistical significance using Fisher's Exact Test (one tailed test, alternative hypothesis = greater), and corresponding p-values were corrected for multiple comparisons using Benjamini/Hochberg procedure.

Gene expression scoring

All gene expression scores were calculated from the h5ad scanpy object as the average expression of all genes in a provided list using the following function in python:

```
obj.raw.X[:,obj.raw.var.index.isin(genes)].mean(1)
```

The following scores were calculated using this method:

ISG score - M8.3:Type 1 Interferon module genes from Altman et al⁵³.

NFKB Pathway Score - BioCarta NFKB Pathway genes obtained from GSEA MSigDB⁵⁴.

Full gene lists are provided in Table S4.

Coexpression analysis

Cells co-expressing *IL1B* and *ISG15* were selected based on *IL1B* expression > 0.5 and *ISG15* expression > 1.487142. The threshold for *ISG15* was determined by the 75% quantile of all healthy control cells within CD14⁺ monocytes, CD16⁺ monocytes, and DCs. Cells were annotated as positive for one or both genes based on whether their expression exceeded these thresholds.

snATAC-seq data processing

snATAC-seq reads were aligned (10x Genomics GRCh38 reference 2020-A) and processed using Cell Ranger ATAC v2.1.0⁵⁵. High quality single nucleus data was selected based on the following criteria: percent of reads within exclusion list regions < 5%, nucleosome signal < 4, percent of fragments in peaks > 15%, number of peak region fragments > 3000, percent fragments at transcription start sites > 10%, and percent mitochondrial read fragments < 10%.

Multiplets were identified by applying AMULET⁵⁶ on each sample independently using FDR < 5%. Multiplets were excluded in downstream analyses to better identify multiplet clusters containing multiplets not captured by AMULET. All multiplets identified by AMULET were excluded after first pass filtering to account for homotypic multiplets.

To define a unified set of peaks (genomic regions) for clustering, individual sample peaks from Cell Ranger ATAC were combined by merging peaks if they overlapped by 1 base pair. Peaks with lengths < 20bp; > 10,000bp, falling on chromosome Y, or represented by fewer than 4 samples were excluded from further analysis. Read count matrices were generated from the remaining peaks for each sample.

Read count matrices were concatenated and normalized by applying a python reimplementation of the term frequency inverse document frequency (TF-IDF) normalization method in Signac⁵⁷. Scanpy objects were generated using this matrix, and singular value decomposition (SVD) of the combined TF-IDF normalized matrix was performed using the *pca* function in Scanpy⁴⁷ with *zero_center = False* to perform truncated SVD.

To measure read counts at transcription start sites (TSS) and gene bodies, gene activity scores were computed using a python reimplementation of gene activity score calculations in Signac⁵⁷. Transcription start site and transcription termination sites from UCSC hg38 Refflat database⁵⁸ were used as gene references. Quantifications included reads within the gene body and 2000 base pairs upstream from the transcription start sites.

snATAC-seq label transfer from scRNA-seq

Nuclei/cells from snATAC-seq and scRNA-seq were divided into 4 lineages: 1) myeloid, 2) CD4⁺ T, 3) NK, CD8⁺ and cytotoxic T, and 4) B cells based on gene activity scores and gene expression values respectively. Within each lineage, cluster annotations from scRNA-seq were transferred onto snATAC-seq cells using *FindTransferAnchors* with *reduction='CCA'* and *TransferData* functions in Signac (version 1.7.0)⁵⁷ and Seurat (version 4.1.1)⁵⁹. Nuclei were then assigned scRNA-seq annotations based on highest probability scores. Based on these annotations, clusters in snATAC-seq data were assigned to reflect the majority of cell predictions within the cluster.

Differential accessibility analysis

Aggregated raw read count matrices were obtained for each annotated subset using peaks called for the respective subset to define the genomic regions used in these matrices. Small subsets were merged (e.g., cDC1s with cDC2s etc) as necessary to increase cell numbers. For each comparison, samples with fewer than 50 cells in the respective population were excluded. Peaks were excluded if fewer than 3 samples had reads > 0. Sample and gene filtered count matrices were then normalized using *filterByExpr* and *calcNormFactors* functions in EdgeR (version 3.36.0)^{50–52}. Differential accessibility analyses were performed using *estimateDisp* and *glmQLFTest* functions, using batch, sex, and age as covariates. All pairwise comparisons between clinical groups as well as combined Healthy, COVID-19 (moderate and severe), and RSV (mild, moderate and severe) comparisons were performed for each annotated subset that had enough samples remaining after filtering to run EdgeR.

Nearest expressed gene identification

Transcription start sites from UCSC hg38 Refflat database⁵⁸ (Downloaded April 2023) were used for identifying nearest expressed gene targets. TSS positions were excluded if corresponding genes did not have expression values > 0 for any sample within a given PBMC subset.

Epigenetic ISG scoring

Differentially accessible peaks in CD14⁺ or CD16⁺ monocytes were selected based on if they were opening with infection and if their nearest expressed gene was among interferon modules from Altman et al⁵³: M10.1:Interferon, M13.17:Interferon, M8.3:Type 1 Interferon, M15.127:Interferon, M15.64:Interferon, M15.86:Interferon. Epigenetic ISG scores were calculated as the average batch corrected log₂ counts per million (CPM) for the selected peaks.

Epigenetic ISG scoring in convalescent COVID-19 adults

Adult healthy, mild convalescent COVID-19 and severe convalescent COVID-19 CD14⁺ monocyte paired end ATAC-seq reads from Cheong et al²¹ (GSE196990) were processed using the ATAC-seq pipeline available at <https://github.com/UcarLab/ATAC-seq>. Epigenetic ISG scores were then calculated as the average log₂ CPM counts using the same regions for epigenetic ISG scores identified in infants.

NFKB ChromVAR Score:

NFKB ChromVAR scores were calculated as the mean of the following ChromVAR deviation scores: MA0105.4_NFKB1, MA0778.1_NFKB2, MA0101.1_REL and MA0107.1_RELA .

Domains of opening chromatin (DORC)

Cells between scRNA-seq and snATAC-seq from the same sample were paired using the *pairCells* function in FigR⁶⁰ version 0.1.0 with the following parameters: *keepUnique = True*, *max_multimatch = 5*, *min_subgraph_size = 60*. The *search_range* parameter was adjusted between 0.05–0.25 as necessary for the function to successfully finish, taking the pairing with the highest search_range as the final pairing. Cell pairings were then filtered by cell annotations such that pairs with consistent cell type annotations between scRNA-seq and snATAC-seq were kept and all other pairs were excluded. Using inferred cell pairings, DORC scores were obtained with FigR by applying *runGenePeakcorr*, *dorcJPlot*, and *getDORCScores* methods and using *pvalZ < 0.05* and *cutoff = 8* to filter correlations and DORCs.

Transcription factor motif binding site accessibility

Transcription factor motif binding sites accessibility deviations were calculated using chromVAR version 1.16.0²³. For each PBMC subset, genomic regions for chromVAR analysis were selected by extending MACS2 summit locations ± 250 base pairs (bp). Read count matrices were then generated based on single nucleus read counts within these regions. TF motif deviations were then calculated using *computeDeviations* in chromVAR, using motifs from *getJasparMotifs()*, (CORE set JASPAR 2016⁶¹, homo sapiens).

Motifs were selected based on TFs with expression > 0 within the respective PBMC subset. Kruskal-Wallis test was applied on median motif deviation scores for each sample across clinical groups and p-values were adjusted for multiple comparisons within each PBMC subset using Benjamini/Hochberg procedure. Finally, significant motifs were selected using p_{adj} values < 0.1.

Motif detection

The *annotatePeaks.pl* function in HOMER version 4.11.1⁶² was used to find instances of motifs within peaks. The *findMotifsGenome.pl* function in HOMER was used for determining motifs enriched for

specific genomic regions. In both analyses, JASPAR-vertebrate (2020)⁶³ motifs filtered for homo sapiens were used as known motifs. Detection thresholds for position weight matrices (PWMs) used in HOMER were calculated as half of the score for perfect matching: $\sum \frac{\log\left(\frac{\max(p)}{0.25}\right)}{2}$ where p is the probability for one nucleotide in a motif.

Log2 CPM matrix Batch Correction

Log2 counts per million (CPM) matrices for differential expression and differential accessibility analysis were corrected with the *ComBat* function of SVA version 3.51.0⁶⁴, using batch as a covariate.

Use of large language models

Large language models including ChatGPT and Copilot were used for writing assistance including grammar check and revising text written by authors.

Declarations

DATA AVAILABILITY

Data can be viewed at the following: <https://covidrsvinfants.jax.org>. Processed data is available on GEO: GSE283746 (token: uzkvsmymppqjtmv) for scRNA-seq, GSE283744 (token: wdkhaccizpmltgn) for snATAC-seq. Raw read data will be made available on dbGAP upon acceptance of the manuscript.

CODE AVAILABILITY

Figure code is available on Zenodo DOI: 10.5281/zenodo.14455083. Data processing code is available on github: <https://github.com/UcarLab/COVID-RSV-Infants>

Acknowledgements

We thank JAX Genomic Technologies and Single Cell cores for their help with generating the sequencing data. We thank Olivia Bart for help with dbGAP data upload. We thank members of the Ucar lab for critical feedback during the progress of the study. This study was made possible by generous financial support of the National Institutes of Health (NIH) grants under award number - U01 AI131386 (to O.R., J.B.), U19 AI168632 (O.R., V.P., D.U.), U01 AI165452 (to D.U.). Opinions, interpretations, conclusions, and recommendations are solely the responsibility of the authors and do not necessarily represent the official views of the National Institutes of Health (NIH).

Author contributions

J.B., O.R., D.U designed the study and raised the funds. J.B., O.R., D.U. co-supervised the study. A.M and O.R coordinated the clinical sample collection and integration with genomics data. A.T. led the data analyses. D.N., V.P., S.P., S.Z.J. helped with data analyses and data interpretation. Z.X. coordinated and generated cytokine data. R.M. generated genomics data. A.T. and D.U. wrote the paper. All authors revised the manuscript and helped with data interpretation.

ETHICS DECLARATION

At the time of the study, J.F.B. was a member of the BOD and SAB of Neovacs and Ascend Biopharma, and a SAB member of Cue Biopharma. A.M. has received research grants from Merck, fees for participation in advisory boards from Pfizer, Merck, Sanofi-Pasteur, Moderna, Enanta, Astra-Zeneca and fees for lectures from Pfizer, Sanofi-Pasteur and Astra-Zeneca. O.R. has received research grants from the Bill & Melinda Gates Foundation and Merck; and fees for participation in advisory boards from Merck, Sanofi-Pasteur, Pfizer and Moderna; and fees for lectures from Pfizer, Merck and Sanofi-Pasteur. None of these fees were related to the research described in this manuscript.

References

1. Wildenbeest, J. G. *et al.* The burden of respiratory syncytial virus in healthy term-born infants in Europe: a prospective birth cohort study. *The Lancet Respiratory Medicine* 11, 341–353 (2023).
2. Rostad, C. A. *et al.* The burden of respiratory syncytial virus infections among children with sickle cell disease. *Pediatric Blood & Cancer* 68, e28759 (2021).
3. Hall, C. B., Simões, E. A. F. & Anderson, L. J. Clinical and epidemiologic features of respiratory syncytial virus. *Curr Top Microbiol Immunol* 372, 39–57 (2013).
4. Lloyd, C. M. & Saglani, S. Early-life respiratory infections and developmental immunity determine lifelong lung health. *Nat Immunol* 24, 1234–1243 (2023).
5. Li, Y. *et al.* Global, regional, and national disease burden estimates of acute lower respiratory infections due to respiratory syncytial virus in children younger than 5 years in 2019: a systematic analysis. *The Lancet* 399, 2047–2064 (2022).
6. Scheltema, N. M. *et al.* Global respiratory syncytial virus-associated mortality in young children (RSV GOLD): a retrospective case series. *The Lancet Global Health* 5, e984–e991 (2017).
7. Shi, T. *et al.* Global, regional, and national disease burden estimates of acute lower respiratory infections due to respiratory syncytial virus in young children in 2015: a systematic review and modelling study. *The Lancet* 390, 946–958 (2017).
8. Nziza, N. *et al.* Longitudinal humoral analysis in RSV-infected infants identifies pre-existing RSV strain-specific G and evolving cross-reactive F antibodies. *Immunity* 57, 1681–1695.e4 (2024).

9. Götzinger, F. *et al.* COVID-19 in children and adolescents in Europe: a multinational, multicentre cohort study. *The Lancet Child & Adolescent Health* 4, 653–661 (2020).
10. Ruckwardt, T. J., Morabito, K. M. & Graham, B. S. Determinants of early life immune responses to RSV infection. *Current Opinion in Virology* 16, 151–157 (2016).
11. Mejias, A. *et al.* Whole Blood Gene Expression Profiles to Assess Pathogenesis and Disease Severity in Infants with Respiratory Syncytial Virus Infection. *PLoS Med* 10, e1001549 (2013).
12. Heinonen, S. *et al.* Immune profiles provide insights into respiratory syncytial virus disease severity in young children. *Sci. Transl. Med.* 12, eaaw0268 (2020).
13. Zivanovic, N. *et al.* Single-cell immune profiling reveals markers of emergency myelopoiesis that distinguish severe from mild respiratory syncytial virus disease in infants. *Clinical & Translational Med* 13, e1507 (2023).
14. Wimmers, F. *et al.* Multi-omics analysis of mucosal and systemic immunity to SARS-CoV-2 after birth. *Cell* 186, 4632–4651.e23 (2023).
15. Nehar-Belaid, D. *et al.* Immune perturbations induced by SARS-CoV2 in infants vary with disease severity and differ from adults' responses. Preprint at <https://doi.org/10.21203/rs.3.rs-5176621/v1> (2024).
16. Sinha, S. *et al.* Dexamethasone modulates immature neutrophils and interferon programming in severe COVID-19. *Nat Med* 28, 201–211 (2022).
17. Knoll, R. *et al.* The life-saving benefit of dexamethasone in severe COVID-19 is linked to a reversal of monocyte dysregulation. *Cell* 187, 4318–4335.e20 (2024).
18. García, C. *et al.* Decreased Innate Immune Cytokine Responses Correlate With Disease Severity in Children With Respiratory Syncytial Virus and Human Rhinovirus Bronchiolitis. *Pediatric Infectious Disease Journal* 31, 86–89 (2012).
19. Mella, C. *et al.* Innate Immune Dysfunction is Associated with Enhanced Disease Severity In Infants with Severe Respiratory Syncytial Virus Bronchiolitis. *The Journal of Infectious Diseases* 207, 564–573 (2013).
20. Zhang, W. *et al.* Caspase-8 in inflammatory diseases: a potential therapeutic target. *Cell Mol Biol Lett* 29, 130 (2024).
21. Cheong, J.-G. *et al.* Epigenetic memory of coronavirus infection in innate immune cells and their progenitors. *Cell* 186, 3882–3902.e24 (2023).
22. Ma, S. *et al.* Chromatin Potential Identified by Shared Single-Cell Profiling of RNA and Chromatin. *Cell* 183, 1103–1116.e20 (2020).
23. Schep, A. N., Wu, B., Buenrostro, J. D. & Greenleaf, W. J. chromVAR: inferring transcription-factor-associated accessibility from single-cell epigenomic data. *Nat Methods* 14, 975–978 (2017).
24. Stein, N. *et al.* IFNG-AS1 Enhances Interferon Gamma Production in Human Natural Killer Cells. *iScience* 11, 466–473 (2019).

25. Wong, P. *et al.* T-BET and EOMES sustain mature human NK cell identity and antitumor function. *Journal of Clinical Investigation* 133, e162530 (2023).
26. Cerapio, J. P. *et al.* Single-Cell RNAseq Profiling of Human $\gamma\delta$ T Lymphocytes in Virus-Related Cancers and COVID-19 Disease. *Viruses* 13, 2212 (2021).
27. Rijkers, G., Vervenne, T. & Van Der Pol, P. More bricks in the wall against SARS-CoV-2 infection: involvement of $\gamma\delta$ T cells. *Cell Mol Immunol* 17, 771–772 (2020).
28. Lei, L. *et al.* The phenotypic changes of $\gamma\delta$ T cells in COVID-19 patients. *J Cellular Molecular Medi* 24, 11603–11606 (2020).
29. Fries, G., Gassen, N. & Rein, T. The FKBP51 Glucocorticoid Receptor Co-Chaperone: Regulation, Function, and Implications in Health and Disease. *IJMS* 18, 2614 (2017).
30. Tay, M. Z., Poh, C. M., Rénia, L., MacAry, P. A. & Ng, L. F. P. The trinity of COVID-19: immunity, inflammation and intervention. *Nat Rev Immunol* 20, 363–374 (2020).
31. Taveras, J. *et al.* Type III Interferons, Viral Loads, Age, and Disease Severity in Young Children With Respiratory Syncytial Virus Infection. *The Journal of Infectious Diseases* 227, 61–70 (2022).
32. Reilly, R. B. *et al.* An altered natural killer cell immunophenotype characterizes clinically severe pediatric RSV infection. *Sci. Transl. Med.* 16, eado6606 (2024).
33. Aberle, J. H. *et al.* Reduced Interferon- γ Expression in Peripheral Blood Mononuclear Cells of Infants with Severe Respiratory Syncytial Virus Disease. *Am J Respir Crit Care Med* 160, 1263–1268 (1999).
34. Sparks, R. *et al.* Influenza vaccination reveals sex dimorphic imprints of prior mild COVID-19. *Nature* 614, 752–761 (2023).
35. Zar, H. J. *et al.* Early-life respiratory syncytial virus disease and long-term respiratory health. *The Lancet Respiratory Medicine* 12, 810–821 (2024).
36. Mejias, A. *et al.* Risk of childhood wheeze and asthma after respiratory syncytial virus infection in full-term infants. *Pediatric Allergy Immunology* 31, 47–56 (2020).
37. Openshaw, P. J. M., Dean, G. S. & Culley, F. J. Links between respiratory syncytial virus bronchiolitis and childhood asthma: clinical and research approaches: *The Pediatric Infectious Disease Journal* 22, S58–S65 (2003).
38. Tian, Y., Sette, A. & Weiskopf, D. Cytotoxic CD4 T Cells: Differentiation, Function, and Application to Dengue Virus Infection. *Front. Immunol.* 7, (2016).
39. Guo, L., Liu, X. & Su, X. The role of TEMRA cell-mediated immune senescence in the development and treatment of HIV disease. *Front. Immunol.* 14, 1284293 (2023).
40. Garcia-Mauriño, C. *et al.* Viral Load Dynamics and Clinical Disease Severity in Infants With Respiratory Syncytial Virus Infection. *J Infect Dis* 219, 1207–1215 (2019).
41. Mertz, C. *et al.* Severe Acute Respiratory Syndrome Coronavirus 2 RNAemia and Clinical Outcomes in Children With Coronavirus Disease 2019. *J Infect Dis* 225, 208–213 (2022).
42. Nevola, K. *et al.* OlinkAnalyze: Facilitate Analysis of Proteomic Data from Olink. 4.0.2 <https://doi.org/10.32614/CRAN.package.OlinkAnalyze> (2022).

43. Zheng, G. X. Y. *et al.* Massively parallel digital transcriptional profiling of single cells. *Nat Commun* 8, 14049 (2017).
44. Young, M. D. & Behjati, S. SoupX removes ambient RNA contamination from droplet-based single-cell RNA sequencing data. *GigaScience* 9, gaaa151 (2020).
45. Wolock, S. L., Lopez, R. & Klein, A. M. Scrublet: Computational Identification of Cell Doublets in Single-Cell Transcriptomic Data. *Cell Systems* 8, 281–291.e9 (2019).
46. Campello, R. J. G. B., Moulavi, D. & Sander, J. Density-Based Clustering Based on Hierarchical Density Estimates. in *Advances in Knowledge Discovery and Data Mining* (eds. Pei, J., Tseng, V. S., Cao, L., Motoda, H. & Xu, G.) vol. 7819 160–172 (Springer Berlin Heidelberg, Berlin, Heidelberg, 2013).
47. Wolf, F. A., Angerer, P. & Theis, F. J. SCANPY: large-scale single-cell gene expression data analysis. *Genome Biol* 19, 15 (2018).
48. Korsunsky, I. *et al.* Fast, sensitive and accurate integration of single-cell data with Harmony. *Nat Methods* 16, 1289–1296 (2019).
49. Alquicira-Hernandez, J. & Powell, J. E. *Nebulosa* recovers single-cell gene expression signals by kernel density estimation. *Bioinformatics* 37, 2485–2487 (2021).
50. Chen, Y., Lun, A. T. L. & Smyth, G. K. From reads to genes to pathways: differential expression analysis of RNA-Seq experiments using Rsubread and the edgeR quasi-likelihood pipeline. *F1000Res* 5, 1438 (2016).
51. McCarthy, D. J., Chen, Y. & Smyth, G. K. Differential expression analysis of multifactor RNA-Seq experiments with respect to biological variation. *Nucleic Acids Research* 40, 4288–4297 (2012).
52. Robinson, M. D., McCarthy, D. J. & Smyth, G. K. edgeR : a Bioconductor package for differential expression analysis of digital gene expression data. *Bioinformatics* 26, 139–140 (2010).
53. Altman, M. C. *et al.* Development of a fixed module repertoire for the analysis and interpretation of blood transcriptome data. *Nat Commun* 12, 4385 (2021).
54. Subramanian, A. *et al.* Gene set enrichment analysis: A knowledge-based approach for interpreting genome-wide expression profiles. *Proc. Natl. Acad. Sci. U.S.A.* 102, 15545–15550 (2005).
55. Satpathy, A. T. *et al.* Massively parallel single-cell chromatin landscapes of human immune cell development and intratumoral T cell exhaustion. *Nat Biotechnol* 37, 925–936 (2019).
56. Thibodeau, A. *et al.* AMULET: a novel read count-based method for effective multiplet detection from single nucleus ATAC-seq data. *Genome Biol* 22, 252 (2021).
57. Stuart, T., Srivastava, A., Madad, S., Lareau, C. A. & Satija, R. Single-cell chromatin state analysis with Signac. *Nat Methods* 18, 1333–1341 (2021).
58. Nassar, L. R. *et al.* The UCSC Genome Browser database: 2023 update. *Nucleic Acids Research* 51, D1188–D1195 (2023).
59. Hao, Y. *et al.* Integrated analysis of multimodal single-cell data. *Cell* 184, 3573–3587.e29 (2021).

60. Kartha, V. K. *et al.* Functional inference of gene regulation using single-cell multi-omics. *Cell Genomics* 2, 100166 (2022).
61. Mathelier, A. *et al.* JASPAR 2016: a major expansion and update of the open-access database of transcription factor binding profiles. *Nucleic Acids Res* 44, D110–D115 (2016).
62. Heinz, S. *et al.* Simple Combinations of Lineage-Determining Transcription Factors Prime cis-Regulatory Elements Required for Macrophage and B Cell Identities. *Molecular Cell* 38, 576–589 (2010).
63. Fornes, O. *et al.* JASPAR 2020: update of the open-access database of transcription factor binding profiles. *Nucleic Acids Research* gkz1001 (2019) doi:10.1093/nar/gkz1001.
64. Jeffrey T. Leek, W. E. J. E. sva. Bioconductor <https://doi.org/10.18129/B9.BIOC.SVA> (2017).

Figures

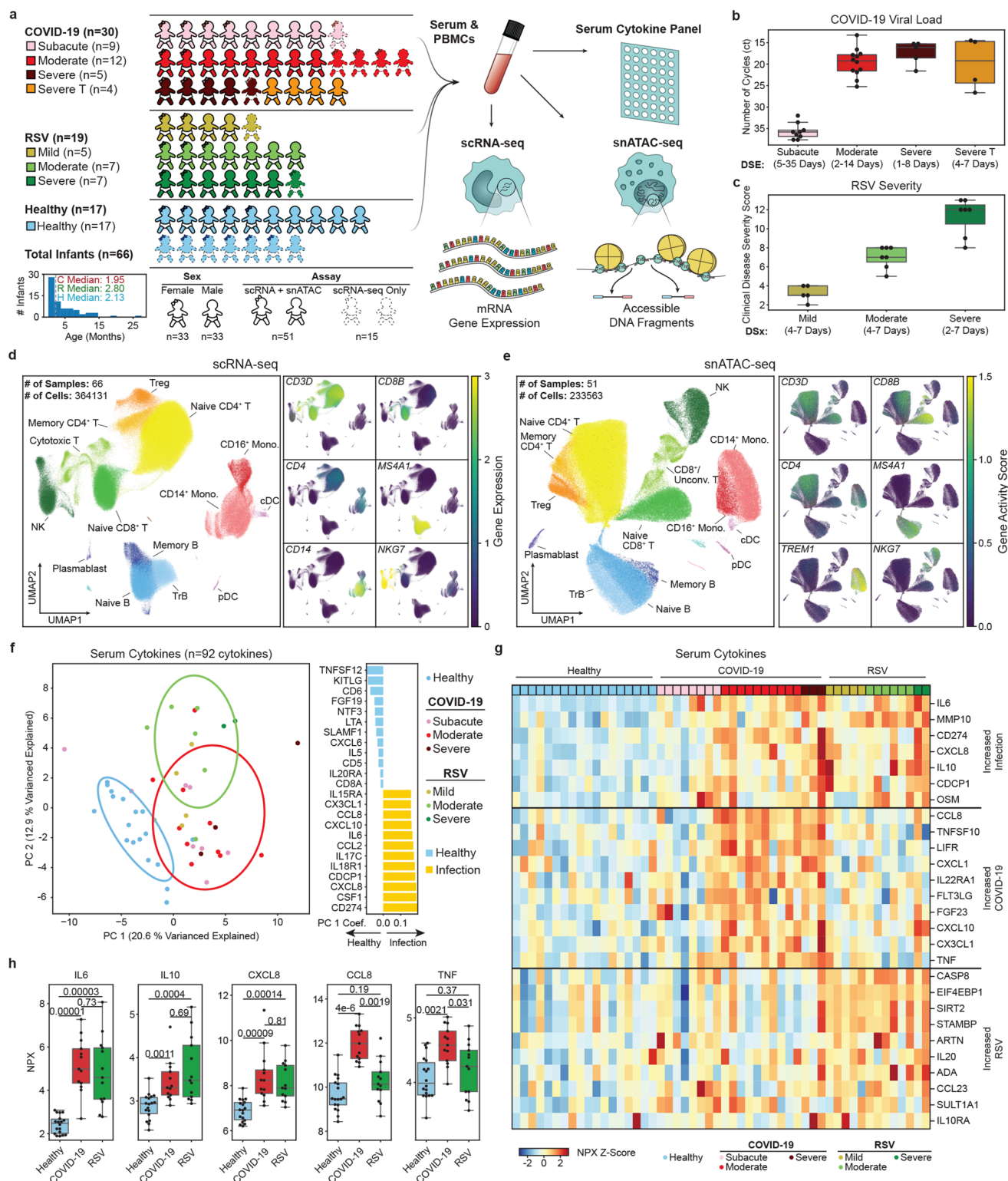


Figure 1

Study design and data overview.

a, Summary of study design. SARS-CoV-2 and RSV sample numbers by disease severity and dexamethasone treatment. Histogram shows age distribution for all infants with median ages for healthy, COVID-19 (moderate and severe) and RSV (mild, moderate, and severe). PBMCs were sequenced

using scRNA-seq and snATAC-seq. Serum samples were profiled using Olink 96 inflammation panel. **b**, Viral loads determined by the number of cycles (ct) required to detect SARS-CoV-2. **c**, RSV disease severity determined by an established clinical disease severity score (CDSS). **d,e**, UMAPs displaying all PBMCs for scRNA-seq and snATAC-seq modalities with respective cell lineage markers: gene expression for scRNA-seq and gene activity scores for snATAC-seq. **f**, (left) Scatterplot of the first two principle components of 92 serum cytokines. (right) Top and bottom cytokines showing the most significant coefficients contributing to PC1. **g**, Heatmap of the top increasing serum cytokine concentrations in infected infants. **h**, Boxplots of select cytokines showing specific examples of shared and SARS-CoV-2 specific increases in proinflammatory cytokines. Adjusted p-values in **h** were calculated using Dunn's test for multiple comparisons.

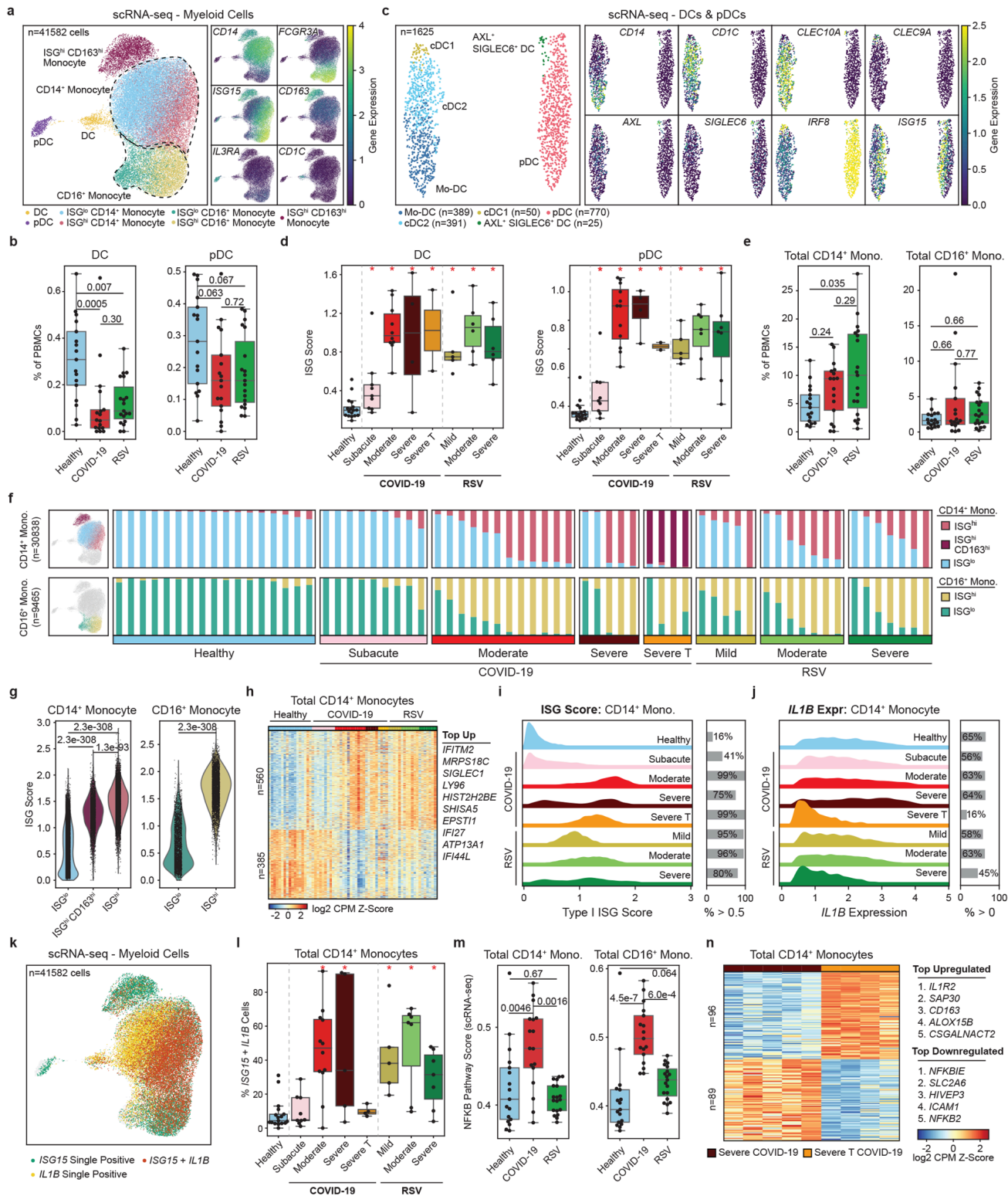


Figure 2

Reduced DC and pDC frequencies and upregulation of ISGs in myeloid cells.

a, UMAP of myeloid cells with marker genes describing CD14⁺ and CD16⁺ monocytes (*CD14* and *FCGR3A*), CD163^{hi} monocytes (*CD163*), DCs (*CD1C*) and pDCs (*IL3RA*). Monocyte clusters separated into ISG^{hi} (*ISG15*) and ISG^{lo} states. **b**, Pairwise comparisons of total DC and pDC frequencies as a

percentage of total PBMCs. **c**, Clustering of DCs and pDCs describing Mo-DCs (*CD14*), cDC1s (*CLEC9A*), cDC2s (*CLEC10A*) and AXL+ SIGLEC6+ DCs (*AXL* and *SIGLEC6*). **d**, Healthy control comparisons of ISG scores with clinical groups. **e**, Pairwise comparisons of total CD14⁺ monocyte and total CD16⁺ monocyte frequencies as a percentage of total PBMCs. **f**, Relative frequencies of CD14⁺ monocyte and CD16⁺ monocyte for ISG^{hi}, ISG^{lo}, and CD163^{hi} cell states. **g**, Pairwise comparisons of ISG scores for CD14⁺ and CD16⁺ monocyte with respect to cell state. **h**, Heatmap of combined healthy vs COVID-19 (moderate and severe) and healthy vs RSV (mild, moderate and severe) differentially expressed genes and top differentially expressed genes in CD14⁺ monocytes. **i,j**, Ridge plots of ISG scores and *IL1B* expression in CD14⁺ monocytes for all clinical groups. **k**, UMAP of cells expressing or co-expressing *ISG15* and/or *IL1B*. **l**, Healthy control comparisons of CD14⁺ monocytes co-expressing *ISG15* and *IL1B* as a percent of total CD14⁺ monocytes. **m**, Pairwise comparisons of NFκB pathway scores for total CD14⁺ and CD16⁺ monocytes. **n**, Heatmap of differentially expressed genes in CD14⁺ monocytes between severe and severe T COVID-19 infant groups. Statistical tests for all pairwise comparisons between healthy controls, COVID-19 (moderate and severe untreated) and RSV (mild, moderate and severe) and monocyte subsets were calculated using Dunn's test of multiple comparisons (panels **b,e,g,m**). Statistical tests for healthy control comparisons across clinical groups were calculated using Mann-Whitney rank sum tests followed by Benjamini Hochberg multiple hypothesis correction (panels **d,l**). Significant comparisons to healthy controls ($p_{\text{adj}} < 0.05$) are indicated by a red asterisk.

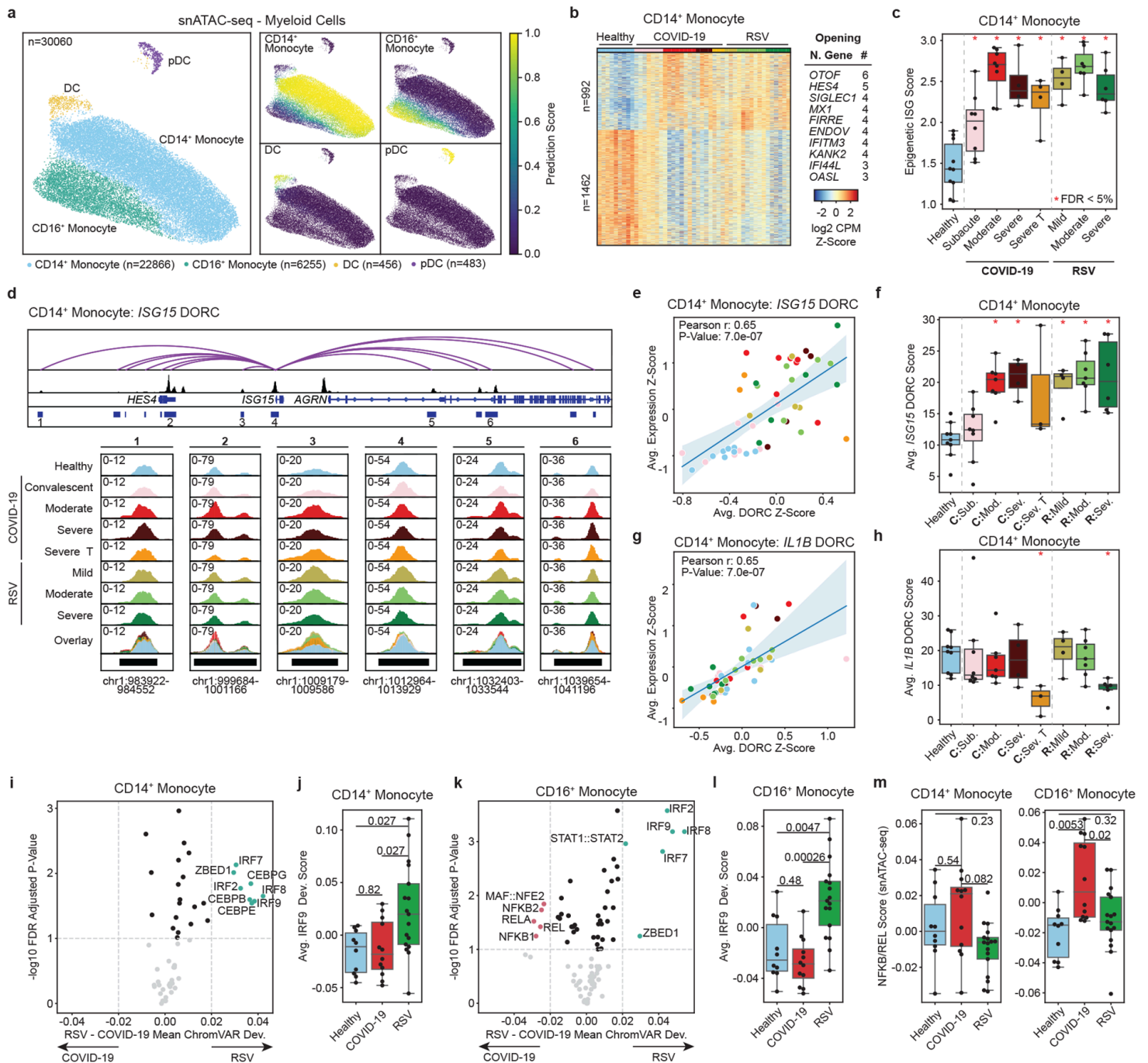


Figure 3

Chromatin remodeling of ISGs and IRFs in monocytes.

a, UMAP of myeloid subsets in snATAC-seq with label transfer prediction scores from scRNA-seq annotations. **b**, Heatmap of combined healthy vs COVID-19 (moderate and severe) and healthy vs RSV (mild, moderate and severe) differentially accessible peaks alongside the genes with the greatest number of nearby peaks in CD14⁺ monocytes. **c**, Epigenetic ISG scores based on opening peaks near ISGs in CD14⁺ monocytes. **d**, Genome browser example of *ISG15* DORC. Arcs indicate significant correlations between accessibility and *ISG15* expression. **e**, Pearson correlation of *ISG15* DORC z-scores and *ISG15* expression z-scores. **f**, Healthy control comparisons of *ISG15* DORC scores across clinical

groups. **g**, Pearson correlation of *IL1B* DORC z-scores and *IL1B* expression z-scores. **h**, Healthy control comparisons of *IL1B* DORC z-scores across clinical groups. **i**, Volcano plot of significant transcription factors comparing COVID-19 (moderate and severe) and RSV (mild, moderate and severe) groups in CD14⁺ monocytes. **j**, Pairwise comparisons of IRF9 chromVAR deviation scores in CD14⁺ monocytes. **k**, Volcano plot of significant transcription factors comparing COVID-19 (moderate and severe) and RSV (mild, moderate and severe) groups in CD16⁺ monocytes. **l**, Pairwise comparisons of IRF9 chromVAR deviation scores in CD16⁺ monocytes. **m**, Pairwise comparisons of NFkB/REL scores derived from chromVAR deviations. Statistical tests for pairwise comparisons between healthy controls, COVID-19 (moderate and severe) and RSV (mild, moderate and severe) were calculated using Dunn's test of multiple comparisons (panels **j,l,m**). Statistical tests for healthy control comparisons across clinical groups were calculated using Mann-Whitney rank sum tests followed by Benjamini Hochberg multiple hypothesis correction (panels **c,f,h**). Significant comparisons to healthy controls ($p_{\text{adj}} < 0.05$) are indicated by a red asterisk.

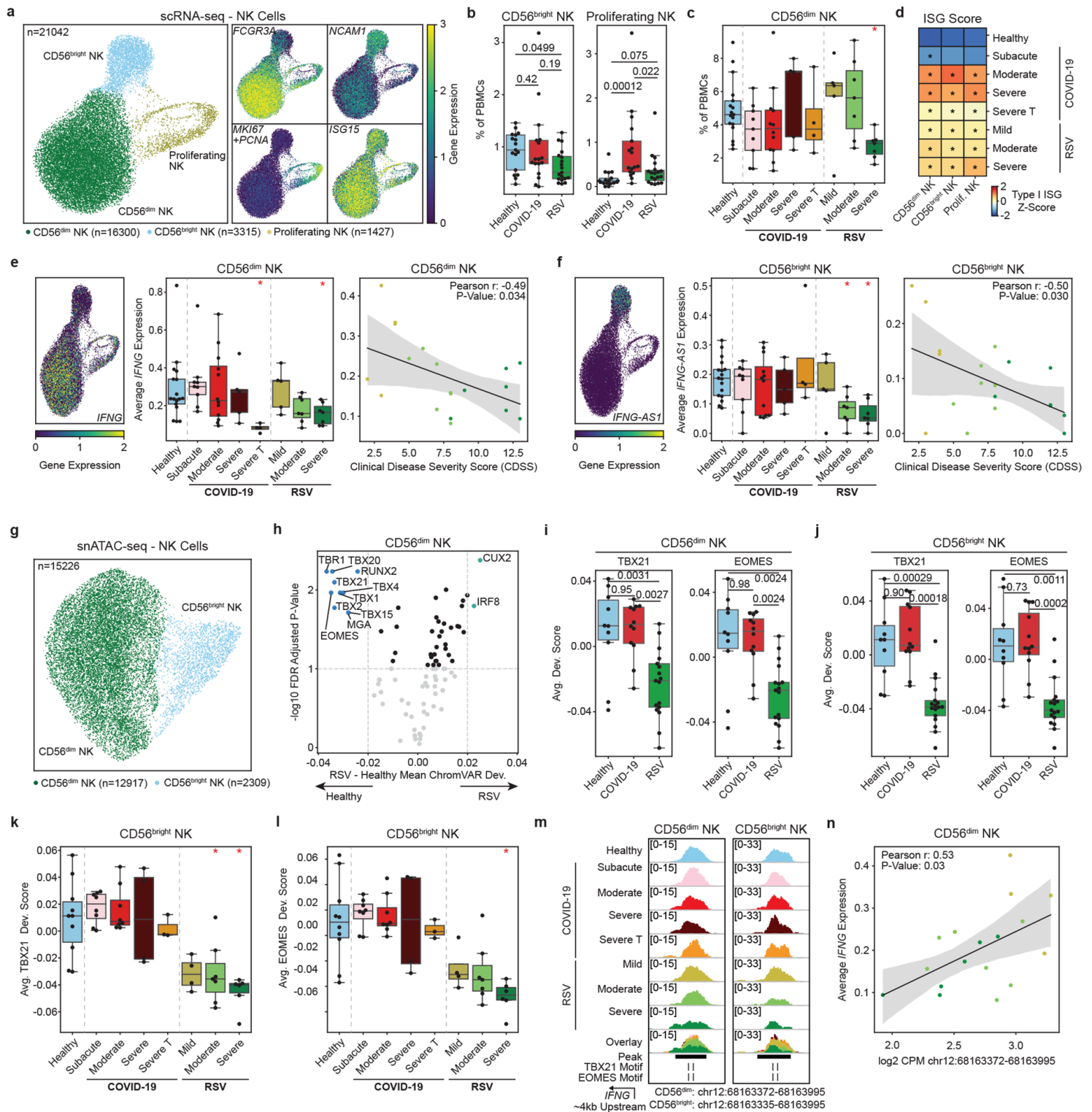


Figure 4

Reduced NK frequencies, *IFNG* expression, and TBET/EOMES binding site accessibility in RSV.

a, UMAP of NK cells and marker genes describing CD56^{dim} NK (*FCGR3A* and low *NCAM1*), CD56^{bright} NK (*NCAM1*), and proliferating NK (*MKI67*). **b**, Pairwise comparisons of CD56^{bright} and proliferating NK cell frequencies as a percentage of total PBMCs. **c**, Healthy control comparisons to clinical groups for

CD56^{dim} NK cell frequencies. **d**, Heatmap of ISG scores for NK cell populations and clinical groups. Asterisks denote significant differences with healthy controls. **e,f**, (left) UMAPs of *IFNG/IFNG-AS1* expression. (center) Healthy control comparisons to clinical groups for *IFNG/IFNG-AS1* expression in CD56^{dim} NK/CD56^{bright} NK cells. (right) Pearson correlation of *IFNG* expression and *IFNG-AS1* expression with clinical disease severity scores. **g**, UMAP of NK subsets in snATAC-seq with prediction scores from label transfer with scRNA-seq annotation. **h**, Volcano plot of statistically significant transcription factors comparing infants with RSV (mild, moderate and severe) to healthy controls in CD56^{dim} NK cells. **i,j**, Pairwise comparisons of TBX21 and EOMES chromVAR deviation scores for CD56^{dim} NK/CD56^{bright} NK cells. **k,l**, Healthy control comparisons of TBX21 and EOMES chromVAR deviation scores for CD56^{bright} NK cells. **m**, Genome browser examples of a peak 4kb upstream of *IFNG* harboring motifs for TBX21 and EOMES in CD56^{dim} and CD56^{bright} NK cells for each clinical group. **n**, Pearson correlation of *IFNG* expression in CD56^{dim} NK cells and peak (panel **m**) accessibility for infants infected with RSV. Scatter plot colors correspond to RSV disease severity in **m**. Statistical tests for pairwise comparisons between healthy controls, COVID-19 (moderate and severe) and RSV (mild, moderate and severe) were calculated using Dunn's test of multiple comparisons (panels **b,i,j**). Statistical tests for healthy control comparisons across clinical groups were calculated using Mann-Whitney rank sum tests followed by Benjamini Hochberg multiple hypothesis correction (panels **c,e,f,k,l**). Significant comparisons ($p_{adj} < 0.05$) to healthy controls are indicated by a red asterisk.

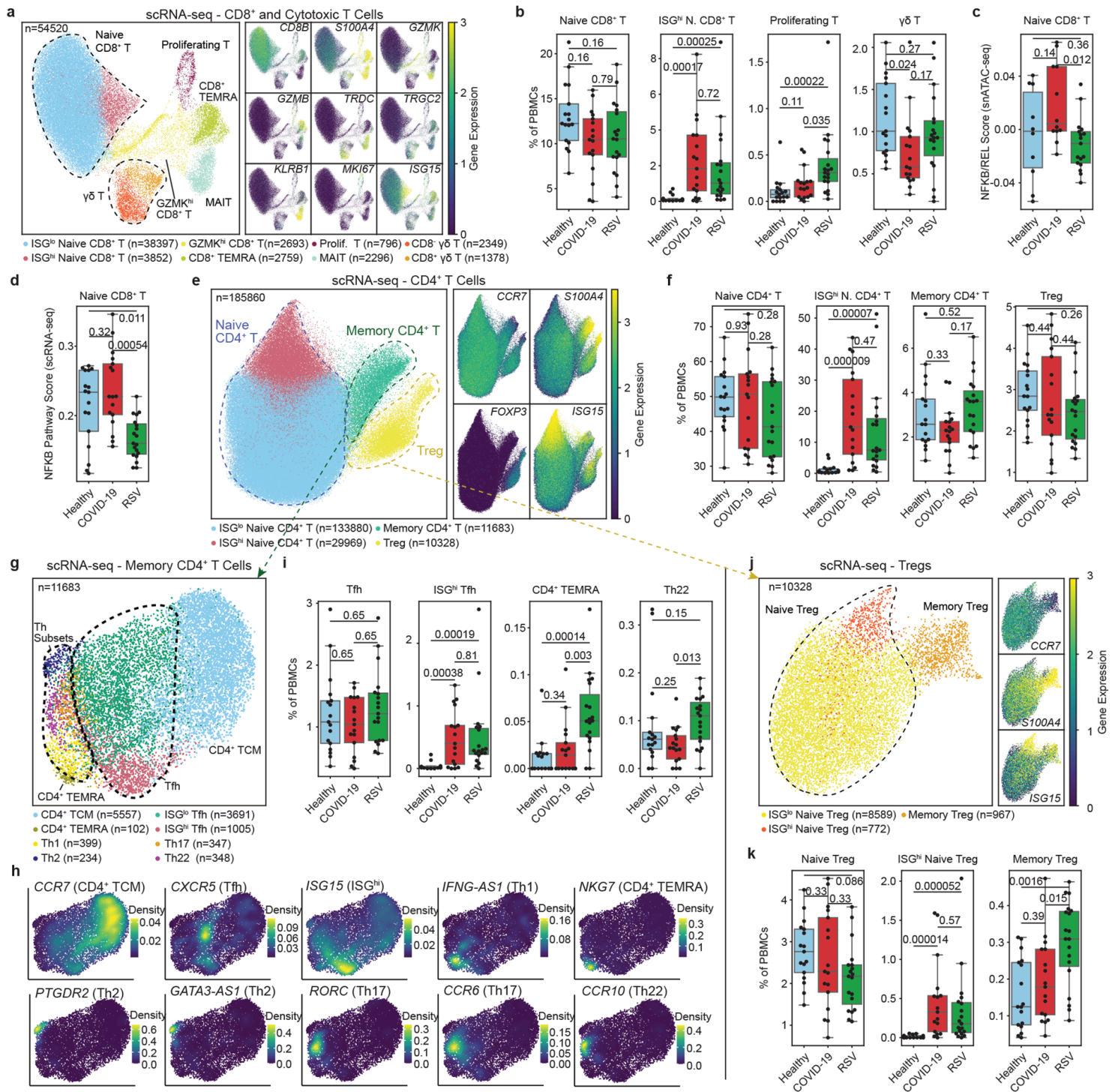


Figure 5

T cell alterations in infants infected with SARS-CoV-2 and RSV.

a, UMAP of CD8⁺ and cytotoxic T cells with marker genes describing ISG^{lo} and ISG^{hi} (ISG15) naive CD8⁺ T, GZMK^{hi} CD8⁺ T (GZMK), CD8⁺ T_{EMRA} (GZMB), proliferating T (MKI67), MAIT (KLRB1), CD8⁺ γδ T (TRDC and TRGC2) and CD8⁺ γδ T (CD8B) cells. **b**, Pairwise comparisons of naive CD8⁺ T, ISG^{hi} CD8⁺ T, proliferating T, and γδ T cell frequencies. **c**, Pairwise comparisons of NFKB/REL scores from snATAC-seq

data in naive CD8⁺ T cells. **d**, Pairwise comparisons of NFkB pathway scores from scRNA-seq data in naive CD8⁺ T cells. **e**, UMAP of CD4⁺ T cells with marker genes describing ISG^{lo} and ISG^{hi} (*ISG15*) naive CD4⁺ T, memory CD4⁺ T (*S100A4*) and T_{reg}(*FOXP3*) cells. **f**, Pairwise comparison of naive CD4⁺ T, ISG^{hi} naive CD4⁺ T, memory CD4⁺ T, and T_{reg} cell frequencies. **g**, UMAP of memory CD4⁺ T clusters. **h**, Density plots of memory CD4⁺ T cluster marker genes. **i**, Pairwise comparisons of Tfh, ISG^{hi} Tfh, CD4⁺ TEMRA and Th22 cell frequencies. **j**, UMAP of T_{reg} cells with marker genes describing ISG^{lo} and ISG^{hi} (*ISG15*) naive T_{reg}, and memory T_{reg} (*S100A4*) cells. **k**, Pairwise comparison of naive Treg, ISG^{hi} Treg and memory Treg cell frequencies. Statistical tests for pairwise comparisons between healthy controls, COVID-19 (moderate and severe) and RSV (mild, moderate and severe) were calculated using Dunn's test of multiple comparisons (panels **b,c,d,f,i,k**).

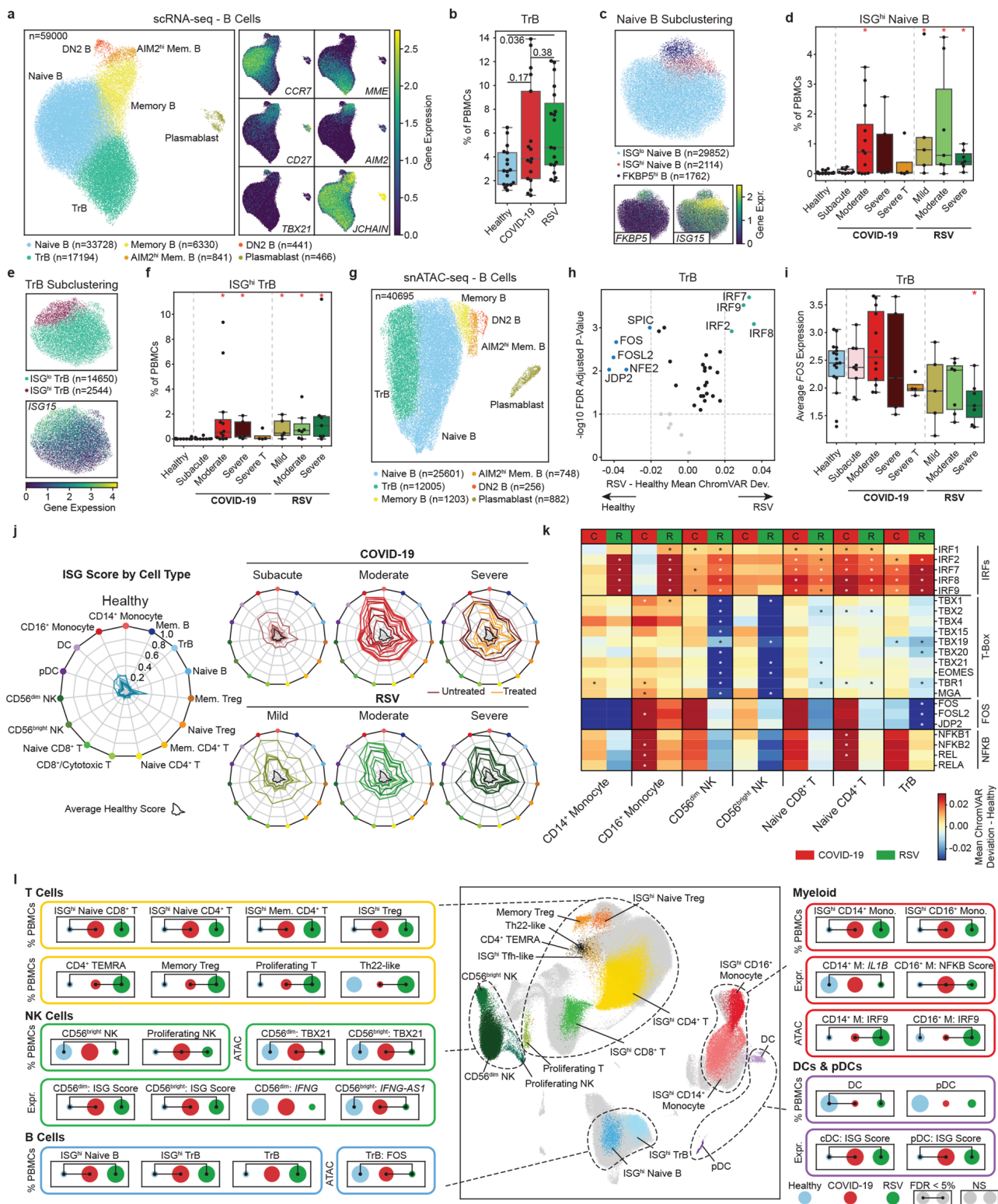


Figure 6

B cell frequencies and summary of SARS-CoV-2 and RSV infections in infants.

a, UMAP of B cells with marker genes describing naive B (*CCR7*), TrB (*MME*), memory B (*CD27*), AIM2^{hi} memory B (*AIM2*), DN2 (*TBX21*) and plasmablast (*JCHAIN*) cells. **b**, Pairwise comparison of TrB cell frequencies. Adjusted p-values were calculated using Dunn's test for multiple comparisons. **c**, UMAP of

naive B cell clusters describing ISG^{lo} and ISG^{hi} (*ISG15*) naive B, and FKB5^{hi} B (*FKBP5*) cells. **d**, Healthy control comparisons of ISG^{hi} naive B cell frequencies. **e**, UMAP of TrB cell clusters describing ISG^{lo} and ISG^{hi} (*ISG15*) TrB cells. **f**, Healthy control comparisons of ISG^{hi} TrB cell frequencies. **g**, UMAP of snATAC-seq B cell clusters annotated by scRNA-seq *via* label transfer. **h**, Volcano plot of significant transcription factors comparing RSV (mild, moderate and severe) and healthy controls in TrB cells. **i**, Healthy control comparisons of *FOS* expression in TrB cells. **j**, Summary of ISG scores (expression) across PBMC subsets identified in this study for each clinical group. **k**, Summary of chromVAR deviation scores for IRF, T-box, FOS, and NFkB related factors in CD14⁺ monocytes, CD16⁺ monocytes, CD56^{dim} NK, CD56^{bright} NK, naive CD8⁺ T, naive CD4⁺ T and TrB subsets. Asterisks denote significant comparisons ($p_{adj} < 0.05$) versus healthy controls using Dunn's test for multiple comparisons. **l**, Highlights of major findings in this study. Dot plots represent the min-max average within healthy controls, COVID-19 (moderate and severe untreated), and RSV (mild, moderate and severe). Lines connecting dots represent significant comparisons using Dunn's test for multiple comparisons. Statistical tests for healthy control comparisons across clinical groups were calculated using Mann-Whitney rank sum tests followed by Benjamini Hochberg multiple hypothesis correction (panels **d,f,i**). Significant comparisons ($p_{adj} < 0.05$) to healthy controls are indicated by a red asterisk.

Supplementary Files

This is a list of supplementary files associated with this preprint. Click to download.

- [ExtendedDataFigs.docx](#)
- [TableS1SampleData.xlsx](#)
- [TableS2CellCompositionData.xlsx](#)
- [TableS3CytokineData.xlsx](#)
- [TableS4Scoring.xlsx](#)
- [TableS5DESummary.xlsx](#)
- [TableS6DASummary.xlsx](#)
- [TableS7DORC.xlsx](#)
- [TableS8ChromVAR.xlsx](#)